

Spectral Probing of Feature Upsamplers in 2D-to-3D Scene Reconstruction

Ling Xiao¹ , Yuliang Xiu² , Yue Chen², Guoming Wang³, and Toshihiko Yamasaki⁴ 

¹ Hokkaido University, Sapporo, Japan
ling@ist.hokudai.ac.jp

² Westlake University, Hangzhou, China
{xiuyuliang, faneggchen}@westlake.edu.cn

³ Zhejiang University, Hangzhou, China
nb21013@zju.edu.cn

⁴ The University of Tokyo, Tokyo, Japan
yamasaki@cvm.t.u-tokyo.ac.jp

Abstract. A typical 2D-to-3D pipeline takes multi-view images as input, where a Vision Foundation Model (VFM) extracts features that are spatially upsampled to dense representations for 3D reconstruction. If dense features across views preserve geometric consistency, differentiable rendering can recover an accurate 3D representation, making the feature upsampler a critical component. Recent learnable upsampling methods mainly aim to enhance spatial details, such as sharper geometry or richer textures, yet their impact on 3D awareness remains underexplored. To address this gap, we introduce a spectral diagnostic framework with six complementary metrics that characterize amplitude redistribution, structural spectral alignment, and directional stability. Across classical interpolation and learnable upsampling methods on CLIP and DINO backbones, we observe three key findings. First, structural spectral consistency (SSC/CSC) is the strongest predictor of NVS quality, whereas High-Frequency Spectral Slope Drift (HFSS) often correlates negatively with reconstruction performance, indicating that emphasizing high-frequency details alone does not necessarily improve 3D reconstruction. Second, geometry and texture respond to different spectral properties: Angular Energy Consistency (ADC) correlates more strongly with geometry-related metrics, while SSC/CSC influence texture fidelity slightly more than geometric accuracy. Third, although learnable upsamplers often produce sharper spatial features, they rarely outperform classical interpolation in reconstruction quality, and their effectiveness depends on the reconstruction model. Overall, our results indicate that reconstruction quality is more closely related to preserving spectral structure than to enhancing spatial detail, highlighting spectral consistency as an important principle for designing upsampling strategies in 2D-to-3D pipelines.

1 Introduction

2D-to-3D scene reconstruction has become a central paradigm for modern 3D modeling. Given multi-view images, a visual backbone extracts image representations that encode spatial correspondences across views. Since patch-based encoders produce coarse representations, feature upsampling is required to recover dense spatial features before constructing neural scene representations such as Gaussian-based models or implicit fields. These representations are optimized through differentiable rendering to enforce geometric and photometric consistency across views, and reconstruction quality is typically evaluated via novel view synthesis (NVS) using metrics such as PSNR, SSIM, and LPIPS.

Feature upsampling therefore plays a critical role in recovering high-resolution representations [9, 11, 15, 25, 29]. Existing methods can be broadly categorized into classical and learnable approaches. Classical techniques include bilinear, nearest-neighbor, bicubic, and Lanczos interpolation, while learnable upsamplers include FeatUp [11], LoftUp [15], LiFT [25], JAFAR [9], and AnyUp [29]. Existing learnable feature upsamplers mainly focus on enhancing spatial details, such as sharper boundaries, richer textures, or higher pixel-level fidelity. However, whether such improvements benefit 3D-aware inference remains largely unexplored. Feat2GS [8] provides a unified and model-agnostic framework for probing the 3D awareness through NVS by disentangling geometry, texture, and overall 3D awareness.

Building on Feat2GS [8], we introduce a spectral diagnosis framework with six complementary metrics that characterize amplitude redistribution, structural spectral alignment, and directional stability, enabling systematic comparison between classical interpolation and learnable upsampling methods. We also introduce Non-cropping Spatial Matching (NSM), a simple baseline that isolates the effect of spatial interpolation. This work investigates three key questions: (1) Is the common assumption of learnable upsamplers, enhancing spatial details such as sharper geometry or richer textures, sufficient for 2D-to-3D reconstruction? (2) Which spectral characteristics most strongly predict 3D awareness across the joint (All), geometry, and texture probing modes? (3) How do classical interpolation methods compare with learnable upsamplers in 3D reconstruction performance? We provide the following contributions:

- We introduce a spectral diagnosis framework that characterizes amplitude redistribution, structural spectral alignment, and directional stability, enabling a systematic analysis of how feature upsampling modifies spectral structure in 2D-to-3D reconstruction pipelines.
- We conduct a systematic comparison of classical interpolation and learnable upsampling methods, analyzing how their spectral transformations influence 3D awareness under overall, geometry-only, and texture-only probing modes.
- Our analysis reveals three key insights that challenge the conventional spatial-detail intuition of feature upsampling: (i) Structural spectral consistency (SSC/CSC) is the strongest predictor of NVS quality, while High-Frequency Spectral Slope Drift (HFSS) often correlates negatively with reconstruction performance; (ii) geometry and texture depend on different spectral

properties: Angular Energy Consistency (ADC) correlates more strongly with geometry-related metrics, whereas SSC/CSC correlate more consistently with texture fidelity; (iii) although learnable upsamplers often produce sharper spatial features, they rarely outperform classical interpolation in reconstruction quality, and their effectiveness depends on the reconstruction model.

2 Related Works

2.1 Feature Upsampling

Many methods have been proposed to convert low-resolution features into high-resolution representations. Classical approaches include bilinear, nearest-neighbor, bicubic, and Lanczos interpolation, which rely on fixed kernels for resampling. Joint Bilateral Upsampling (JBU) [19] refines features using image guidance but may introduce blur and interpolation artifacts. Other directions, such as GAN-based densification [26] and distillation-based upsampling [7], require complex task-specific training pipelines. However, their fixed kernels cannot adapt to image content or feature semantics, often resulting in oversmoothing and limited ability to recover fine spatial structures.

Recent works overcome the limitations of classical methods by learning content-aware upsampling modules that enhance spatial details such as sharper boundaries, richer textures, or higher pixel-level fidelity. LiFT [25] proposes a lightweight ViT-compatible upsampler that fuses image and feature representations through a U-Net-style architecture. FeatUp [11] provides both a fast JBU-based feedforward variant and a per-image implicit variant for sharper detail. LoftUp [15] models upsampling as a coordinate-to-feature mapping with cross-attention for global reasoning. JAFAR [9] formulates upsampling as global attention between high-resolution image features and low-resolution patch features, enabling arbitrary-resolution outputs. AnyUp [29] introduces a feature-agnostic framework with channel-independent projection and window-based attention to generalize across backbone feature types. However, they primarily focus on enhancing spatial details, while largely overlooking whether such enhancements are beneficial for 3D-aware inference. Therefore, systematically analyzing which factors influence overall reconstruction quality, geometry, and texture is crucial for guiding the design of future feature upsamplers.

2.2 Measuring 3D Awareness

Previous studies have examined the 3D awareness of VFMs [4] through tasks such as geometric cue estimation [2, 12, 14, 16, 17, 30], 6D pose estimation [24], spatial reasoning [6], and visual tracking [27]. While these works demonstrate the geometric capability of VFMs, many evaluations focus on coarse spatial reasoning, such as object consistency [5], spatial visual question answering [13, 32], and visual perspective taking [22]. More fine-grained evaluations, including

depth or normal estimation and two-view correspondence [1, 10], typically rely on labeled 3D data, limiting scalability.

Recent work explores probing 3D awareness without explicit 3D supervision. Feat2GS [8] follows this direction by regressing 3D Gaussian Splatting representations from VFM features and evaluating them via novel view synthesis (NVS), enabling dense and label-free probing of 3D awareness. Crucially, it enables disentangled evaluation of overall, geometry-only, and texture-only reconstruction fidelity, providing a controlled testbed for analyzing how different upsampling strategies affect distinct aspects of 3D reconstruction.

3 Methods

3.1 Motivations and Workflow

In 2D-to-3D pipelines, Vision Foundation Models (VFMs) extract patch-level features that must be upsampled into dense maps before pixel-level rendering and scene reconstruction. Feature upsampling therefore influences spatial continuity and local feature relationships, which directly affect the fidelity of reconstructed 3D scene. Despite its importance, the role of feature upsampling in 3D perception remains largely unexplored. Most pipelines rely on simple interpolation such as bilinear upsampling, while recently proposed learnable upsamplers mainly focus on enhancing spatial details such as sharper boundaries or richer textures. However, it remains unclear whether such enhancements are beneficial for 3D-aware inference. To address this gap, we investigate how different upsampling strategies reshape the spectral structure of 2D features and how these spectral changes influence 3D awareness, measured via NVS quality.

The workflow is shown in Fig. 1. Using Feat2GS [8] as the baseline, each input image is resized to a fixed resolution $H \times W$ ($(H = W = 256)$). A VFM extracts the low-resolution feature map $F_{LR} \in \mathbb{R}^{h \times w \times C}$, which is then upsampled to $F_{HR} \in \mathbb{R}^{H \times W \times C}$. To isolate the effect of upsampling, all methods operate on the same F_{LR} and differ only in the transformation from $h \times w$ to $H \times W$. The resulting features are regressed into 3D Gaussian Splatting parameters and optimized via differentiable rendering. To analyze what information is preserved in the upsampled features, we adopt three probing modes that selectively read out Gaussian parameters: **Geometry (G)**: predicts geometric parameters $(\mathbf{x}_i, \alpha_i, \Sigma_i)$; **Texture (T)**: predicts appearance parameters \mathbf{c}_i ; **All (A)**: jointly predicts both geometry and appearance parameters. Here \mathbf{x}_i denotes the 3D position of the i -th Gaussian, α_i its opacity, Σ_i its covariance matrix, and \mathbf{c}_i its appearance parameters.

3.2 Spectral Diagnostics

Feature upsampling not only changes spatial resolution but also modifies the spectral structure of feature representations. In the Fourier domain, it redistributes spectral energy, alters phase relationships, and may introduce orientation-dependent distortions. To systematically characterize these effects, we propose

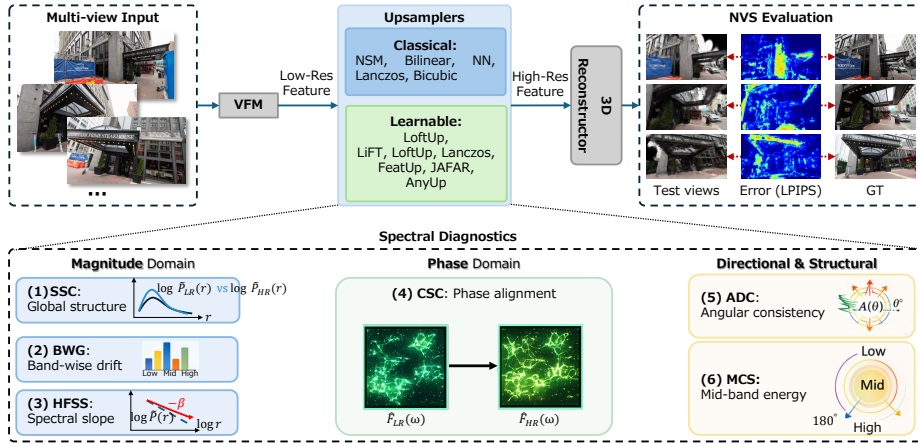


Fig. 1: Overview of the spectral probing pipeline. Feature upsamplers reshape spectral structure, which in turn affects reconstruction quality. Our framework measures this relationship through six spectral diagnostics and NVS evaluation. Specifically, multi-view images are resized to $H \times W$ and encoded into patch-grid features ($h \times w$). Different upsampling strategies produce dense maps at $H \times W$, which are used to regress 3D Gaussian parameters via differentiable rendering. Spectral changes are correlated with NVS quality (PSNR, SSIM, LPIPS) to probe 3D awareness.

six complementary spectral diagnostics. Global Spectral Structure Preservation (SSC) and Band-wise Spectral Drift (BWG) capture global and localized spectral energy redistribution. High-Frequency Spectral Slope Drift (HFSS) measures deviations from the natural decay of high-frequency components. Complex Spectral Coherence (CSC) evaluates phase-aligned structural preservation, while Angular Energy Consistency (ADC) detects orientation-dependent distortions. Mid-band Concentration Stability (MCS) quantifies the stability of mid-frequency structural components. Together, these diagnostics provide complementary perspectives for understanding how spectral transformations induced by upsampling influence downstream 3D reconstruction quality.

Fourier Representation. For a feature map $F \in \{F_{\text{LR}}, F_{\text{HR}}\}$, we compute the 2D Fourier transform

$$\hat{F}(\boldsymbol{\omega}) = \mathcal{F}(F),$$

where $\boldsymbol{\omega} = (\omega_x, \omega_y)$ denotes the spatial frequency coordinate defined on the discrete frequency grid Ω . The power spectrum is defined as

$$P(\boldsymbol{\omega}) = |\hat{F}(\boldsymbol{\omega})|^2. \quad (1)$$

In practice, spectra are computed independently for each feature channel and then aggregated across channels (e.g., by averaging) to obtain a single spectrum per feature map. Applying this transform to F_{LR} and F_{HR} produces spectra $P_{\text{LR}}(\boldsymbol{\omega})$ and $P_{\text{HR}}(\boldsymbol{\omega})$. To summarize the frequency distribution independent of

orientation, we compute a radial spectrum by averaging $P(\boldsymbol{\omega})$ within discrete radial bins defined by $r = \|\boldsymbol{\omega}\|$:

$$\tilde{P}(r) = \mathbb{E}_{\|\boldsymbol{\omega}\| \in [r, r+\Delta r)} P(\boldsymbol{\omega}), \quad (2)$$

where Δr denotes the radial bin width. This operation yields radial spectra $\tilde{P}_{\text{LR}}(r)$ and $\tilde{P}_{\text{HR}}(r)$. All diagnostics below quantify changes between the low-resolution and upsampled spectra.

Magnitude-Based Diagnostics: (1) SSC. SSC measures how well overall frequency allocation is preserved after upsampling, capturing global structural similarity while being insensitive to uniform spectral scaling. We compute Pearson correlation between log radial spectra:

$$SSC = \rho\left(\log \tilde{P}_{\text{LR}}(r), \log \tilde{P}_{\text{HR}}(r)\right), \quad (3)$$

where $\rho(\cdot, \cdot)$ denotes the Pearson correlation coefficient.

Magnitude-Based Diagnostics: (2) BWG. While SSC summarizes global similarity, it may miss localized redistribution across specific frequency ranges. To capture such frequency-selective effects, we introduce BWG, which measures how spectral energy shifts across frequency bands after upsampling. We divide the radial frequency axis into K disjoint bands $\{\mathcal{R}_k\}_{k=1}^K$, where k indexes the band. The energy of band k is computed as

$$E_k^{(\cdot)} = \sum_{r \in \mathcal{R}_k} \tilde{P}_{(\cdot)}(r), \quad (4)$$

where $(\cdot) \in \{\text{LR}, \text{HR}\}$ indicates the spectrum source. We then compare the normalized band energy distributions:

$$BWG = \sum_{k=1}^K \left| \frac{E_k^{\text{LR}}}{\sum_{j=1}^K E_j^{\text{LR}}} - \frac{E_k^{\text{HR}}}{\sum_{j=1}^K E_j^{\text{HR}}} \right|, \quad (5)$$

where j indexes all frequency bands.

Magnitude-Based Diagnostics: (3) HFSS. HFSS measures how strongly upsampling alters the natural spectral decay; large deviations suggest excessive sharpening or smoothing effects. Natural visual signals approximately follow a power-law spectral decay:

$$\tilde{P}(r) \propto r^{-\beta}, \quad (6)$$

where r denotes radial frequency and β represents the spectral decay slope. To estimate β , we perform linear regression in the log-log domain over a predefined high-frequency range:

$$\log \tilde{P}(r) = -\beta \log r + c, \quad (7)$$

where c is a constant. The slope β is obtained via least-squares fitting using radial spectrum samples $\{(r_i, \tilde{P}(r_i))\}$ within the selected high-frequency region. The slope drift introduced by upsampling is then defined as

$$HFSS = |\beta_{\text{HR}} - \beta_{\text{LR}}|. \quad (8)$$

Phase-Based Diagnostic: (4) CSC. Magnitude statistics characterize spectral energy distribution, whereas phase encodes spatial alignment and structural consistency. We therefore evaluate phase-consistent structural preservation using normalized complex spectral coherence between LR and HR spectra:

$$CSC = \left| \frac{\sum_{\omega \in \Omega} \hat{F}_{LR}(\omega) \overline{\hat{F}_{HR}(\omega)}}{\sqrt{\sum_{\omega \in \Omega} |\hat{F}_{LR}(\omega)|^2 \sum_{\omega \in \Omega} |\hat{F}_{HR}(\omega)|^2}} \right|. \quad (9)$$

Directional and Structural Diagnostics: (5) ADC. Radial statistics ignore orientation-dependent distortions. To analyze directional spectral structure, ADC quantifies how well the orientation distribution of spectral energy is preserved after upsampling. We partition the angular domain into bins $\{\mathcal{B}_m\}$, where m indexes the angular bin. The angular energy in bin m is computed as

$$A_m^{(\cdot)} = \sum_{\omega \in \mathcal{B}_m} P_{(\cdot)}(\omega), \quad (10)$$

where $(\cdot) \in \{\text{LR}, \text{HR}\}$. The similarity between angular energy distributions is measured by

$$ADC = \rho(A^{\text{LR}}, A^{\text{HR}}), \quad (11)$$

where

$$A^{\text{LR}} = \{A_m^{\text{LR}}\}_m, \quad A^{\text{HR}} = \{A_m^{\text{HR}}\}_m.$$

Directional and Structural Diagnostics: (6) MCS. Mid-frequency components often encode structural edges and geometric contours. Let \mathcal{R}_{mid} denote the mid-frequency region. The mid-band concentration is defined as

$$MCS = \frac{E_{mid}}{E_{total}}, \quad (12)$$

where

$$E_{mid} = \sum_{r \in \mathcal{R}_{mid}} \tilde{P}(r), \quad E_{total} = \sum_r \tilde{P}(r).$$

The deviation introduced by upsampling is defined as

$$\Delta MCS = |MCS_{\text{HR}} - MCS_{\text{LR}}|. \quad (13)$$

4 Experimental Results

4.1 Experimental Settings

Implementation Details. We evaluate two widely used vision backbones, DINO and CLIP. Both adopt a patch size of 16×16 and provide publicly available pretrained checkpoints for most learnable upsamplers. The input images are resized to 256×256 , which is evenly divisible by the patch size and ensures consistent feature map alignment across backbones.

Table 1: Datasets for Evaluation.

Dataset	Scene Type	Complexity	View Range	Views
LLFF [23]	Indoor	Simple	Small	2
DL3DV [21]	Indoor / Outdoor	Moderate	Medium	5–6
Casual [8]	Daily Scenario	Moderate	Medium	4–7
MipNeRF360 [3]	Unbounded	Moderate	360	6
MVImgNet [31]	Outdoor Object	Moderate	180–360	2–4
T&T [18]	Indoor / Outdoor	High	Large	6

We evaluate both classical interpolation and learnable upsampling methods. The classical baselines include bilinear, nearest-neighbor, bicubic, and Lanczos interpolation. For learnable upsamplers, we adopt publicly available pretrained checkpoints whenever possible, including JAFAR (DINO, CLIP) [9], AnyUp (DINO, CLIP) [29], FeatUp (JBU) (CLIP) [11], LoftUp (CLIP) [15], and LiFT (DINO) [25]. All methods are evaluated within the same framework with identical data processing, feature extraction, and reconstruction settings.

We introduce Non-cropping Spatial Matching (NSM), a simple baseline that isolates the effect of interpolation. Instead of resampling, NSM applies right- and bottom-side zero-padding to match the target resolution (H, W) . Given a low-resolution feature map $\mathbf{F}_{\text{LR}} \in \mathbb{R}^{h \times w \times C}$, NSM produces $\mathbf{F}_{\text{NS}} \in \mathbb{R}^{H \times W \times C}$ as

$$\mathbf{F}_{\text{NS}} = \begin{cases} \mathbf{F}_{\text{LR}}, & \text{if } (h, w) = (H, W), \\ \text{Pad}(\mathbf{F}_{\text{LR}}; (0, W - w, 0, H - h)), & \text{otherwise.} \end{cases} \quad (14)$$

Here $\text{Pad}(\cdot)$ denotes zero-padding along the right and bottom edges to expand the feature map to (H, W) .

Datasets and Metrics. We conduct experiments on six diverse multi-view datasets (Table 1). For each dataset, 2–7 sparse training views are sampled, while test viewpoints are placed farther away to enforce extrapolation. In total, we evaluate 30 scenes. For each scene, spectral diagnostics are computed on all training views and averaged to obtain scene-level statistics. NVS quality is evaluated per scene, and cross-scene correlations between spectral diagnostics and NVS metrics are analyzed to study how frequency-domain characteristics relate to 3D awareness.

We adopt three complementary NVS metrics: PSNR, SSIM, and LPIPS, capturing pixel fidelity, structural similarity, and perceptual similarity, respectively, providing a multi-scale assessment of geometry and appearance consistency across views.

4.2 Experimental Results

Main Results. Tables 2 and 3 report cross-dataset average NVS performance using DUSt3R [28] and MAST3R [20] under three probing modes: All (geometry+texture), Geometry-only, and Texture-only. Under the joint All setting,

Table 2: Cross-dataset average NVS performance using DUST3R [28] as the 3D reconstructor. Results are reported under three probing modes: All (geometry+texture), Geometry-only, and Texture-only. Metrics are averaged over 30 scenes from six datasets. Best results are highlighted in bold.

Feature	Upsamplers	All			Geometry			Texture		
		PSNR \uparrow	SSIM \uparrow	LPIPS \downarrow	PSNR \uparrow	SSIM \uparrow	LPIPS \downarrow	PSNR \uparrow	SSIM \uparrow	LPIPS \downarrow
DINO	NSM	23.62	0.8383	0.1628	18.13	0.7811	0.2212	22.57	0.8204	0.1415
	Bilinear	<u>24.08</u>	0.8400	0.1601	<u>24.32</u>	0.8483	0.1368	22.58	0.8193	0.1413
	NN	23.94	0.8396	0.1606	22.54	0.8214	0.1790	22.71	0.8211	0.1392
	Lanczos	24.07	<u>0.8408</u>	0.1582	24.29	0.8475	0.1342	22.71	<u>0.8215</u>	0.1392
	Bicubic	24.15	0.8416	<u>0.1577</u>	24.36	<u>0.8477</u>	<u>0.1343</u>	22.83	0.8237	0.1370
	LiFT [25]	24.04	0.8389	0.1571	24.16	0.8400	0.1416	22.72	0.8201	0.1398
	JAFAR [9]	23.61	0.8375	0.1630	24.15	0.8416	0.1420	21.52	0.8084	0.1568
	AnyUp [29]	24.04	0.8389	0.1625	24.13	0.8430	0.1401	<u>22.74</u>	0.8209	<u>0.1389</u>
CLIP	NSM	24.33	0.8479	0.1516	19.42	0.7988	0.2084	22.68	0.8210	0.1397
	Bilinear	23.91	0.8403	0.1594	<u>24.21</u>	0.8454	0.1388	22.56	0.8200	0.1409
	NN	24.05	0.8397	0.1592	22.56	0.8209	0.1808	22.62	0.8208	0.1405
	Lanczos	23.90	0.8393	0.1584	24.14	0.8431	0.1391	<u>22.70</u>	<u>0.8211</u>	0.1397
	Bicubic	<u>24.32</u>	<u>0.8468</u>	<u>0.1522</u>	24.13	0.8433	0.1393	22.67	0.8209	0.1399
	LoftUp [15]	24.05	0.8416	0.1601	24.19	0.8450	0.1390	22.75	0.8213	<u>0.1389</u>
	FeatUp [11]	23.95	0.8391	0.1592	24.53	0.8514	0.1301	22.62	0.8207	0.1402
	JAFAR [9]	23.98	0.8401	0.1589	23.93	0.8402	0.1432	21.53	0.8051	0.1570
AnyUp [29]	24.12	0.8416	0.1628	24.19	<u>0.8456</u>	<u>0.1386</u>	<u>22.70</u>	0.8205	0.1388	

Table 3: Cross-dataset average NVS performance using MAST3R [20] as the 3D reconstructor. Results are reported under three probing modes: All (geometry+texture), Geometry-only, and Texture-only. Metrics are averaged over 30 scenes from six datasets. Best results are highlighted in bold.

Feature	Upsamplers	All			Geometry			Texture		
		PSNR \uparrow	SSIM \uparrow	LPIPS \downarrow	PSNR \uparrow	SSIM \uparrow	LPIPS \downarrow	PSNR \uparrow	SSIM \uparrow	LPIPS \downarrow
DINO	NSM	17.93	0.7818	0.2212	17.87	0.7751	0.2256	16.25	0.7120	0.2315
	Bilinear	18.26	0.7628	0.2273	16.68	0.7272	0.2419	15.55	0.6928	0.2571
	NN	17.15	0.7591	0.2384	17.87	<u>0.7688</u>	0.2225	16.25	0.7116	<u>0.2317</u>
	Lanczos	17.78	<u>0.7753</u>	0.2261	<u>17.95</u>	0.7496	0.2196	16.50	0.7151	0.2334
	Bicubic	17.89	0.7580	0.2269	17.69	0.7468	<u>0.2207</u>	<u>16.63</u>	<u>0.7159</u>	0.2322
	LiFT [25]	17.67	0.7628	0.2330	17.62	0.7440	0.2216	15.82	0.7008	0.2433
	JAFAR [9]	17.77	0.7573	0.2270	17.97	0.7475	0.2219	16.66	0.7118	0.2388
	AnyUp [29]	<u>17.95</u>	0.7739	<u>0.2250</u>	17.45	0.7384	0.2284	16.62	0.7163	0.2318
CLIP	NSM	18.02	<u>0.7774</u>	<u>0.2218</u>	18.25	0.7844	0.2148	15.98	0.7015	0.2422
	Bilinear	17.90	0.7498	0.2378	17.38	0.7381	0.2256	16.02	0.7022	0.2429
	NN	18.09	0.7796	0.2206	<u>18.01</u>	<u>0.7641</u>	0.2301	16.37	0.7060	0.2428
	Lanczos	<u>18.15</u>	0.7713	0.2254	17.42	0.7436	0.2264	16.50	0.7151	<u>0.2329</u>
	Bicubic	17.28	0.7453	0.2437	16.95	0.7298	0.2346	15.86	0.6980	0.2464
	LoftUp [15]	17.61	0.7519	0.2317	17.24	0.7366	0.2276	16.04	0.7042	0.2417
	FeatUp [11]	18.16	0.7580	0.2220	17.96	0.7453	<u>0.2192</u>	16.79	0.7168	0.2320
	JAFAR [9]	17.13	0.7438	0.2374	17.64	0.7348	0.2321	16.38	0.7012	0.2461
AnyUp [29]	18.09	0.7706	0.2267	17.73	0.7460	0.2202	<u>16.52</u>	<u>0.7153</u>	0.2331	

Table 4: Per-dataset NVS performance using DUS_t3R [28] with the CLIP backbone on six multi-view datasets under three probing modes: Geometry-only, Texture-only, and All (geometry+texture). Best results are highlighted in bold. **More results are provided in the Supplementary Material.**

	LLFF									DL3DV									
	Geometry			Texture			All			Geometry			Texture			All			
	PSNR \uparrow	SSIM \uparrow	LPIPS \downarrow	PSNR \uparrow	SSIM \uparrow	LPIPS \downarrow	PSNR \uparrow	SSIM \uparrow	LPIPS \downarrow	PSNR \uparrow	SSIM \uparrow	LPIPS \downarrow	PSNR \uparrow	SSIM \uparrow	LPIPS \downarrow	PSNR \uparrow	SSIM \uparrow	LPIPS \downarrow	
Upsamplers																			
NSM	19.21	.8350	.1593	24.11	.8904	.0779	<u>25.13</u>	.9028	.0858	18.26	.8207	.1967	20.62	.8334	.1555	<u>22.09</u>	.8616	.1596	
Bilinear	25.05	.9021	<u>.0745</u>	23.96	.8882	.0803	24.99	.8899	.0919	22.27	.8614	.1514	20.86	.8373	.1528	22.00	.8618	<u>.1590</u>	
NN	23.04	.8529	.1256	24.00	.8882	.0802	25.02	.8887	.0923	20.74	.8474	.1712	21.03	.8388	.1520	22.03	.8607	.1598	
Lanczos	24.91	.8996	.0750	24.14	.8906	.0779	24.96	.8880	.0915	<u>22.36</u>	.8609	<u>.1502</u>	20.63	.8329	.1560	21.93	.8604	.1598	
Bicubic	24.93	.9005	.0746	24.11	.8901	.0781	25.22	<u>.9015</u>	<u>.0870</u>	22.20	.8607	.1515	20.59	.8334	.1553	21.77	.8581	.1632	
LoftUp [15]	24.97	.9027	.0761	24.37	.8915	.0769	24.88	.8931	.0941	22.33	<u>.8616</u>	.1518	20.79	.8354	.1545	21.85	.8603	.1607	
FeatUp [11]	<u>25.10</u>	.9080	.0679	24.23	.8913	.0767	25.04	.8885	.0917	22.61	.8666	.1439	20.40	.8314	.1581	21.70	.8570	.1617	
JAFAR [9]	25.07	.9041	.0757	24.39	.8929	.0752	24.96	.8884	.0928	21.98	.8555	.1570	18.54	.8061	.1843	22.19	<u>.8637</u>	.1573	
AnyUp [29]	25.16	<u>.9054</u>	.0757	<u>24.38</u>	<u>.8922</u>	<u>.0756</u>	25.08	.8855	.0972	22.30	.8610	.1528	20.66	.8328	.1555	21.94	.8639	.1605	
	Casual									MipNeRF360									
	Geometry			Texture			All			Geometry			Texture			All			
Upsamplers	PSNR \uparrow	SSIM \uparrow	LPIPS \downarrow	PSNR \uparrow	SSIM \uparrow	LPIPS \downarrow	PSNR \uparrow	SSIM \uparrow	LPIPS \downarrow	PSNR \uparrow	SSIM \uparrow	LPIPS \downarrow	PSNR \uparrow	SSIM \uparrow	LPIPS \downarrow	PSNR \uparrow	SSIM \uparrow	LPIPS \downarrow	
NSM	19.94	.8041	.2258	22.80	.7974	.1736	24.57	.8467	<u>.1825</u>	19.42	.7028	.2843	23.43	.7342	.1709	24.95	.7585	<u>.2090</u>	
Bilinear	24.40	.8424	.1708	22.67	.7961	.1759	23.71	.8427	.1881	<u>24.81</u>	<u>.7576</u>	.1761	23.33	.7341	.1716	24.57	.7490	.2152	
NN	23.07	.8260	.2029	22.70	.7963	.1758	24.50	.8444	.1866	23.34	.7327	.2481	23.28	.7332	.1723	24.56	.7477	.2145	
Lanczos	24.60	.8435	.1708	22.81	<u>.7980</u>	.1732	23.96	.8431	.1876	24.70	.7531	.1779	23.46	<u>.7344</u>	.1709	24.50	.7465	.2133	
Bicubic	24.63	.8433	.1696	22.82	.7973	.1743	<u>24.65</u>	<u>.8460</u>	.1816	24.73	.7531	.1782	<u>23.45</u>	.7348	<u>.1714</u>	<u>24.85</u>	<u>.7577</u>	.2083	
LoftUp [15]	<u>24.75</u>	<u>.8464</u>	<u>.1676</u>	22.87	.7981	<u>.1723</u>	24.66	.8449	.1890	24.67	.7534	.1768	23.29	.7305	.1719	24.59	.7497	.2187	
FeatUp [11]	25.47	.8482	.1580	22.72	.7969	.1754	24.58	.8450	.1861	24.90	.7660	.1643	23.25	.7311	.1728	24.51	.7477	.2137	
JAFAR [9]	24.26	.8453	.1715	23.04	.7977	.1724	24.33	.8446	.1881	24.48	.7490	.1817	21.33	.7076	.2046	24.49	.7483	.2135	
AnyUp [29]	24.31	.8461	.1681	<u>22.92</u>	.7974	.1722	24.09	.8414	.1924	24.78	.7565	<u>.1753</u>	23.26	.7297	.1720	24.62	.7524	.2241	
	MVImgNet									T&T									
	Geometry			Texture			All			Geometry			Texture			All			
Upsamplers	PSNR \uparrow	SSIM \uparrow	LPIPS \downarrow	PSNR \uparrow	SSIM \uparrow	LPIPS \downarrow	PSNR \uparrow	SSIM \uparrow	LPIPS \downarrow	PSNR \uparrow	SSIM \uparrow	LPIPS \downarrow	PSNR \uparrow	SSIM \uparrow	LPIPS \downarrow	PSNR \uparrow	SSIM \uparrow	LPIPS \downarrow	
NSM	18.83	.7728	.2130	21.28	.7947	.1469	24.25	.8257	.1416	20.85	.8574	.1712	23.82	.8760	.1132	<u>25.00</u>	<u>.8924</u>	<u>.1309</u>	
Bilinear	24.09	<u>.8244</u>	<u>.1313</u>	21.06	.7920	.1494	23.82	.8155	.1635	<u>24.65</u>	.8841	.1284	23.51	.8724	.1154	24.38	.8830	.1387	
NN	21.93	.7910	.1944	21.04	.7920	.1493	23.81	.8145	.1637	23.25	.8756	.1425	23.67	.8761	.1132	24.36	.8822	.1386	
Lanczos	23.89	.8208	.1321	21.27	.7945	.1473	23.70	.8147	.1610	24.36	.8805	.1288	23.87	.8762	.1132	24.35	.8831	.1373	
Bicubic	24.02	.8224	.1317	21.25	.7938	.1471	24.25	<u>.8251</u>	<u>.1423</u>	24.30	.8798	.1303	23.80	.8762	.1132	25.16	.8928	.1308	
LoftUp [15]	23.95	.8218	.1332	21.35	<u>.7957</u>	<u>.1455</u>	23.86	.8157	.1607	24.48	.8842	.1282	<u>23.84</u>	<u>.8765</u>	<u>.1123</u>	24.46	.8858	.1377	
FeatUp [11]	24.24	.8343	.1221	<u>21.31</u>	.7959	.1450	23.67	.8145	.1627	24.86	.8854	.1248	23.80	.8777	.1135	24.19	.8819	.1395	
JAFAR [9]	23.69	.8101	.1397	20.03	.7676	.1719	23.64	.8139	.1625	24.11	.8773	.1336	21.87	.8589	.1334	24.29	.8816	.1393	
AnyUp [29]	24.01	.8202	.1339	21.25	.7945	.1458	<u>24.03</u>	.8151	.1691	24.58	<u>.8846</u>	<u>.1260</u>	23.69	.8764	.1119	24.94	.8913	.1336	

classical interpolation methods such as bicubic and Lanczos achieve competitive performance compared with learnable upsampling approaches. Table 4 further reports per-dataset results using the CLIP backbone. Despite dataset-specific variations, similar trends remain consistent across LLFF, DL3DV, Casual, MipNeRF360, MVImgNet, and T&T. More experimental results are provided in the Supplementary Material. Fig. 2 shows visualizations of images synthesized using different upsamplers.

Spectral Diagnostics and Their Relationship with NVS Quality. We visualize the relationship between spectral diagnostics and NVS quality using three complementary analyses. Fig. 3 shows cross-scene Spearman correlations between spectral diagnostics and NVS metrics under the joint All probing setting. More experimental results are provided in the Supplementary Material. To further disentangle geometric and perceptual effects, we introduce two specialized probing modes:

Ground Truth									
	NSM	Bilinear	NN	Lanczos	Bicubic	FeatUp	LoftUp	JAFAR	AnyUp
Geometry									
	SSIM \uparrow : 0.7774	SSIM \uparrow : .7959	SSIM \uparrow : 0.7966	SSIM \uparrow : 0.7921	SSIM \uparrow : 0.7905	SSIM \uparrow : 0.7999	SSIM \uparrow: 0.8077	SSIM \uparrow : 0.7845	SSIM \uparrow : 0.8043
Texture									
	LPIPS \downarrow : 0.1949	LPIPS \downarrow : 0.1831	LPIPS \downarrow : 0.1787	LPIPS \downarrow : 0.1825	<u>LPIPS \downarrow: 0.1754</u>	LPIPS \downarrow : 0.1800	LPIPS \downarrow : .1819	LPIPS \downarrow : 0.1957	LPIPS \downarrow : 0.1755
All									
	SSIM \uparrow : 0.8031 LPIPS \downarrow : 0.2318	SSIM \uparrow : 0.8085 LPIPS \downarrow : 0.2344	SSIM \uparrow : 0.7982 LPIPS \downarrow : 0.2269	SSIM \uparrow : 0.7957 LPIPS \downarrow : 0.2310	SSIM \uparrow: 0.8093 <u>LPIPS \downarrow: 0.2260</u>	SSIM \uparrow : 0.8029 LPIPS \downarrow : 0.2310	SSIM \uparrow : 0.7895 LPIPS \downarrow : 0.2336	SSIM \uparrow : 0.7828 LPIPS \downarrow : 0.2674	SSIM \uparrow : 0.8082 LPIPS \downarrow: 0.2235

Fig. 2: NVS visualizations using CLIP+DUST3R [28]. Classical interpolation methods often achieve performance comparable to learned upsamplers. Best and second-best results are shown in bold and underlined, respectively.

AG (geometry). For each scene, we quantify geometric consistency by the mean relative pose error RPE_{mean} computed from the optimized camera poses. Since RPE_{mean} is a lower-is-better quantity, we convert it to a unified higher-is-better geometry score as $AG = -RPE_{\text{mean}}$.

AT (texture/appearance). We measure perceptual appearance using LPIPS from the NVS evaluation. Because LPIPS is also lower-is-better, we similarly convert it to a unified higher-is-better appearance score: $AT = -LPIPS$.

To quantify geometry–texture asymmetry, we further compute the influence gap $\Delta = |\rho_G| - |\rho_T|$, where ρ_G and ρ_T denote correlations under AG and AT probing, respectively (Fig. 5). Positive values indicate stronger geometry coupling, whereas negative values indicate stronger texture coupling. Overall, we have three key findings.

1) **Structural spectral consistency predicts NVS quality, while HFSS shows negative correlations, challenging the common assumption that enhancing high-frequency details improves reconstruction.** Across backbone–upsampler configurations, the structural diagnostics SSC and CSC consistently exhibit the strongest positive correlations with reconstruction quality under the joint All setting (Fig. 3). This indicates that preserving global spectral structure and coherence is crucial for stable 2D-to-3D reconstruction. Although other factors such as magnitude redistribution (ADC/BWG/MCS) also contribute, NVS performance mainly depends on the joint preservation of spectral magnitude distribution and structural coherence. Notably, HFSS frequently shows negative correlations with overall reconstruction quality (All)(Fig. 3), as well as with geometry (AG) and texture (AT) (Fig. 4). This indicates that stronger high-frequency spectral drift is often associated with worse reconstruction performance. These observations suggest that simply emphasizing high-frequency details, a common objective of many learnable upsampling methods, does not necessarily improve 3D reconstruction.

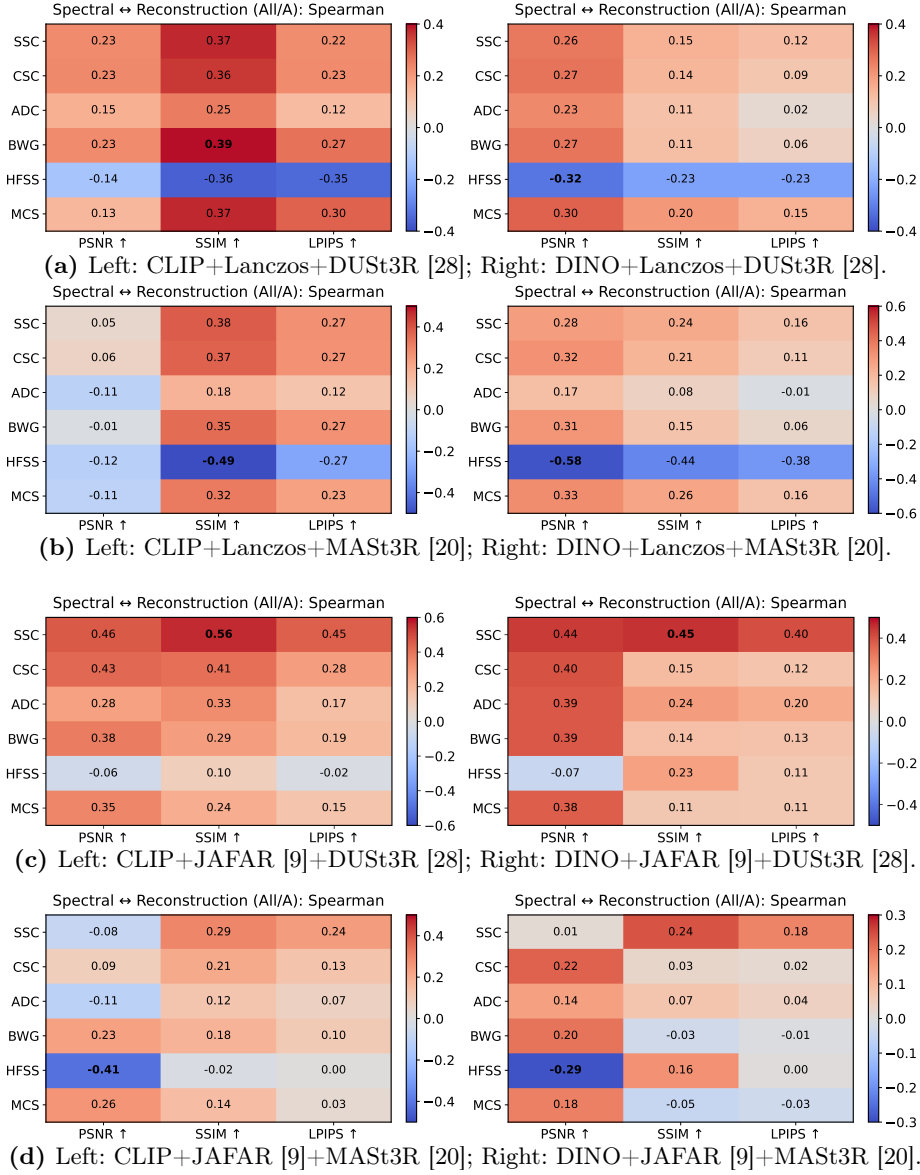


Fig. 3: Spectral–reconstruction correlations. Each row shows the Spearman correlation heatmap. Results of other upsamplers are provided in the Supplementary Material.

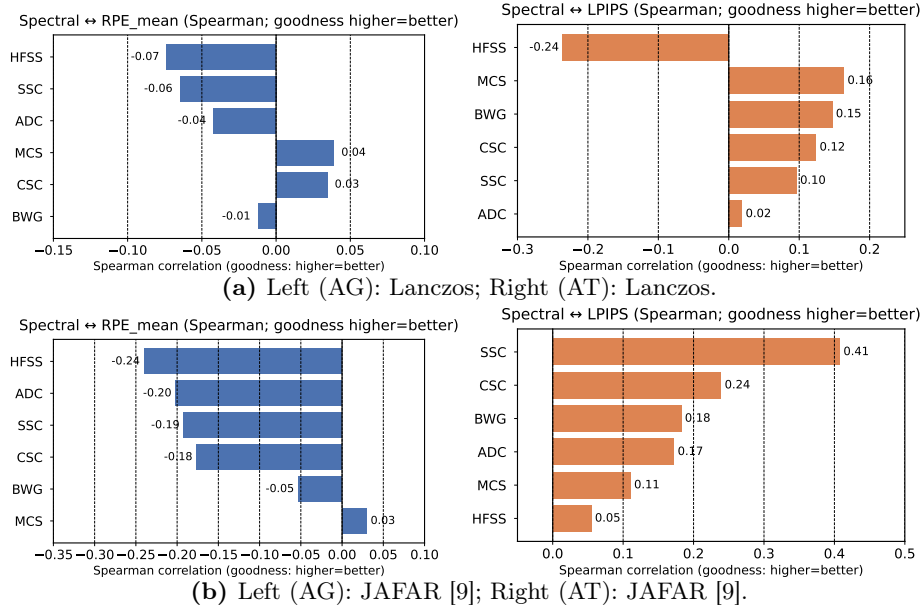


Fig. 4: Spectral diagnostics under geometry-only (AG) and texture-only (AT) settings (CLIP+DUST3R [28]). **Additional results are in the Supplementary Material.**

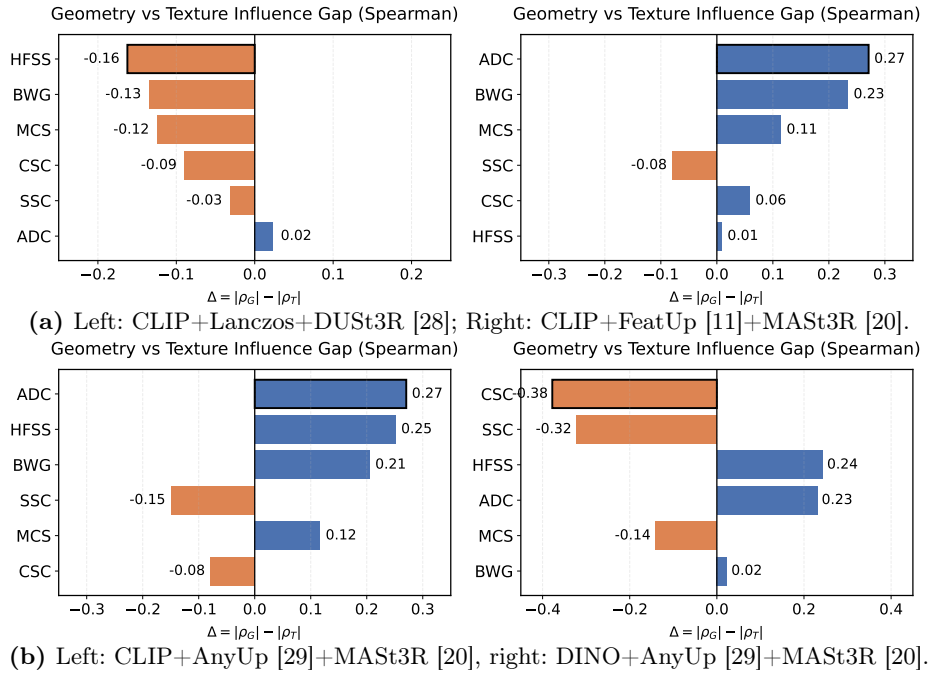


Fig. 5: Geometry-texture influence gap. **Results of other upsamplers are provided in the Supplementary Material.**

2) **Geometry and texture respond differently to spectral perturbations.** The AG and AT analyses reveal distinct sensitivities of geometry and appearance to spectral variations (Fig. 5). In particular, the amplitude distribution metric ADC frequently exhibits positive influence gaps across multiple interpolation and learned upsampling methods, indicating stronger coupling with geometry-related reconstruction metrics. However, the magnitude of this effect varies depending on the backbone encoder and the 3D reconstructor. In contrast, the structural spectral consistency metrics (SSC and CSC) tend to influence texture fidelity slightly more than geometric accuracy but this trend can also be affected by the backbone encoder and the 3D reconstructor.

3) **Classical interpolation remains competitive with learnable upsamplers, and upsampling effectiveness depends on the reconstruction model.** Although learnable upsamplers reshape spectral statistics (Fig. 3), their reconstruction improvements are often modest and backbone-dependent (Tables 2, 3, and 4). Classical interpolation methods such as Lanczos and Bicubic frequently achieve comparable NVS performance with learnable upsamplers, highlighting that spectral–reconstruction interactions, rather than spatial detail enhancement alone, largely determine the final reconstruction quality. Furthermore, with DUS3R [28] (Table 2), the simple NSM baseline yields the weakest geometry-only performance. In contrast, with MAST3R [20] (Table 3), NSM becomes more competitive and can outperform several interpolation baselines, suggesting that the impact of upsampling depends on how the reconstructor utilizes feature representations.

5 Limitations and Future Work

This work is primarily evaluation-oriented and does not explicitly incorporate these findings into the design of feature upsamplers. Future work will build on these insights to develop upsamplers that better preserve cross-view structural consistency. In particular, integrating spectral diagnostics into the training objectives of learnable upsamplers may guide frequency redistribution and phase alignment, improving the robustness of 2D-to-3D representations.

6 Conclusion

We investigate how feature upsampling influences 3D awareness in 2D-to-3D pipelines and examine whether the common assumption of existing state-of-the-art learnable upsamplers truly benefits 3D reconstruction. To analyze this effect, we introduce a spectral diagnostic framework that decomposes upsampling-induced changes into magnitude redistribution, phase alignment, and directional structure. We systematically evaluate classical interpolation and learnable upsampling methods under identical settings and analyze their correlations with NVS quality. Our experiments reveal three key findings. First, structural spectral consistency (SSC/CSC) is the strongest predictor of NVS quality, whereas HFSS often shows negative correlations with reconstruction performance. This

indicates that stronger high-frequency spectral drift tends to degrade reconstruction quality, suggesting that simply emphasizing high-frequency details does not necessarily benefit 3D reconstruction. Second, the amplitude distribution metric ADC frequently exhibits stronger coupling with geometry-related reconstruction metrics, whereas structural spectral consistency metrics (SSC and CSC) tend to correlate more strongly with texture fidelity. These effects may vary depending on the backbone encoder and the 3D reconstructor. Third, learnable upsamplers do not consistently outperform classical interpolation, and the effectiveness of upsampling depends on the reconstruction model.

Supplementary: Spectral Probing of Feature Upsamplers in 2D-to-3D Scene Reconstruction

Ling Xiao¹ , Yuliang Xiu² , Yue Chen², Guoming Wang³, and Toshihiko Yamasaki⁴ 

¹ Hokkaido University, Sapporo, Japan
ling@ist.hokudai.ac.jp

² Westlake University, Hangzhou, China
{xiuyuliang, faneggchen}@westlake.edu.cn

³ Zhejiang University, Hangzhou, China
nb21013@zju.edu.cn

⁴ The University of Tokyo, Tokyo, Japan
yamasaki@cvm.t.u-tokyo.ac.jp

1 More Experimental Results

1.1 Detailed Results Across Different Datasets.

More detailed per-dataset NVS evaluation results are reported in Tables 1, 2, and 3. These tables present results on six multi-view datasets (LLFF, DL3DV, Casual, MipNeRF360, MVImgNet, and T&T) under the three probing modes: Geometry-only (G), Texture-only (T), and All (A).

Table 1 reports results using DUS_t3R with the DINO backbone. Across datasets, classical interpolation methods such as Bilinear, Bicubic, and Lanczos generally provide stable performance, while the no-upsampling baseline (NSM) consistently yields weaker geometry results. This confirms that dense spatial interpolation is important for maintaining geometric consistency when DUS_t3R is used as the 3D reconstructor.

Tables 2 and 3 present the corresponding results using MAS_t3R with DINO and CLIP backbones. Compared with DUS_t3R, the performance differences between upsampling strategies become smaller, and the NSM baseline often remains competitive across datasets. This observation further supports that the effectiveness of feature upsampling is reconstructor-dependent.

Despite dataset-specific variations, several consistent trends can be observed. First, classical interpolation methods remain strong baselines and often achieve performance comparable to learned upsampling methods. Second, the relative ranking of upsampling strategies is broadly consistent across datasets.

1.2 Correlation Heatmaps

Additional Spearman correlation heatmaps under the joint (All, A) setting for other upsampling methods are shown in Figs. 1, and 2. Each heatmap reports cross-scene correlations between spectral diagnostics (goodness-aligned)

Table 1: Per-dataset NVS performance using DUST3R [28] with the DINO backbone. Results are reported on six multi-view datasets (LLFF, DL3DV, Casual, MipNeRF360, MVImgNet, and T&T) under three probing modes: Geometry-only, Texture-only, and All (geometry + texture). We evaluate PSNR (\uparrow), SSIM (\uparrow), and LPIPS (\downarrow). NSM denotes the no-upsampling baseline. Best results within each dataset and probing mode are highlighted in bold.

	LLFF									DL3DV								
	Geometry			Texture			All			Geometry			Texture			All		
Upsamplers	PSNR \uparrow	SSIM \uparrow	LPIPS \downarrow	PSNR \uparrow	SSIM \uparrow	LPIPS \downarrow	PSNR \uparrow	SSIM \uparrow	LPIPS \downarrow	PSNR \uparrow	SSIM \uparrow	LPIPS \downarrow	PSNR \uparrow	SSIM \uparrow	LPIPS \downarrow	PSNR \uparrow	SSIM \uparrow	LPIPS \downarrow
NSM	18.54	.8298	.1655	23.04	.8804	.0949	21.97	.8657	.1230	16.11	.7658	.2303	20.98	.8408	.1498	<u>22.22</u>	<u>.8628</u>	<u>.1575</u>
Bilinear	25.01	<u>.9061</u>	<u>.0696</u>	23.97	.8879	.0804	24.08	.8791	.1052	22.62	.8681	.1453	20.92	.8395	.1509	22.16	.8619	.1582
NN	22.63	.8501	.1275	24.00	.8882	.0803	24.02	.8797	.1050	20.93	.8489	.1695	20.91	.8394	.1513	21.72	.8570	.1620
Lanczos	25.04	.9060	.0703	24.12	.8903	<u>.0782</u>	25.04	<u>.8884</u>	<u>.0904</u>	22.58	.8662	.1458	20.95	.8399	.1506	22.00	.8618	.1582
Bicubic	25.01	.9067	.0695	24.09	.8899	.0783	25.14	.8898	.0910	<u>22.61</u>	<u>.8674</u>	<u>.1456</u>	21.00	<u>.8402</u>	<u>.1502</u>	22.32	.8660	.1549
LiFT [25]	25.03	.8999	.0752	<u>24.18</u>	<u>.8900</u>	<u>.0782</u>	24.88	.8854	.0892	22.41	.8607	.1515	20.56	.8311	.1564	22.12	.8621	.1581
JAFAR [9]	25.43	.9041	.0751	22.10	.8745	.1035	22.15	.8703	.1207	21.99	.8538	.1596	<u>20.99</u>	<u>.8402</u>	.1504	21.94	.8595	.1588
AnyUp [29]	<u>25.17</u>	.9026	.0758	24.36	.8914	.0763	<u>25.06</u>	.8842	.0959	21.89	.8558	.1558	20.62	.8334	.1556	21.83	.8605	.1607
	Casual									MipNeRF360								
	Geometry			Texture			All			Geometry			Texture			All		
Upsamplers	PSNR \uparrow	SSIM \uparrow	LPIPS \downarrow	PSNR \uparrow	SSIM \uparrow	LPIPS \downarrow	PSNR \uparrow	SSIM \uparrow	LPIPS \downarrow	PSNR \uparrow	SSIM \uparrow	LPIPS \downarrow	PSNR \uparrow	SSIM \uparrow	LPIPS \downarrow	PSNR \uparrow	SSIM \uparrow	LPIPS \downarrow
NSM	16.88	.7773	.2446	<u>23.16</u>	.7981	<u>.1732</u>	24.09	.8439	.1854	18.59	.6927	.2926	<u>23.25</u>	<u>.7310</u>	.1727	24.75	.7527	.2164
Bilinear	<u>25.10</u>	.8452	.1643	23.09	.7970	.1763	<u>24.84</u>	<u>.8448</u>	.1848	24.91	.7621	<u>.1711</u>	23.14	.7292	.1742	24.70	.7516	.2168
NN	22.96	.8265	.2000	23.14	.7968	.1748	24.48	.8445	.1847	23.22	.7316	.2453	23.15	.7291	.1740	24.73	.7526	.2175
Lanczos	24.87	.8439	.1627	23.15	.7980	.1735	24.44	.8447	.1841	24.86	<u>.7613</u>	.1700	23.16	.7282	.1738	24.81	<u>.7529</u>	.2156
Bicubic	25.08	.8440	<u>.1633</u>	23.12	.7987	<u>.1732</u>	24.44	.8436	.1873	<u>24.90</u>	.7610	.1716	<u>23.25</u>	.7309	.1726	<u>24.80</u>	<u>.7529</u>	.2139
LiFT [25]	25.18	.8423	.1716	23.08	.7962	.1737	25.07	.8467	.1841	24.59	.7482	.1799	23.37	.7313	.1714	24.33	.7430	.2111
JAFAR [9]	24.98	.8436	.1695	20.67	.7780	.2032	24.63	.8433	<u>.1842</u>	24.61	.7516	.1802	21.35	.7087	.2032	24.66	.7530	<u>.2143</u>
AnyUp [29]	24.67	<u>.8448</u>	.1677	23.33	<u>.7986</u>	.1715	24.48	.8426	.1883	24.78	.7564	.1757	23.22	.7306	<u>.1724</u>	24.63	.7504	.2220
	MVImgNet									T&T								
	Geometry			Texture			All			Geometry			Texture			All		
Upsamplers	PSNR \uparrow	SSIM \uparrow	LPIPS \downarrow	PSNR \uparrow	SSIM \uparrow	LPIPS \downarrow	PSNR \uparrow	SSIM \uparrow	LPIPS \downarrow	PSNR \uparrow	SSIM \uparrow	LPIPS \downarrow	PSNR \uparrow	SSIM \uparrow	LPIPS \downarrow	PSNR \uparrow	SSIM \uparrow	LPIPS \downarrow
NSM	18.69	.7734	.2132	21.22	.7949	.1460	24.07	.8167	.1630	19.97	.8474	.1809	23.74	.8773	.1125	24.61	<u>.8882</u>	.1313
Bilinear	23.72	.8271	.1406	21.05	.7904	.1497	23.92	.8142	.1635	24.57	.8812	.1298	23.30	.8717	.1161	24.78	<u>.8882</u>	.1322
NN	22.32	.7948	.1908	21.04	.7905	.1504	23.95	.8155	.1624	23.19	.8766	.1412	<u>24.00</u>	<u>.8824</u>	<u>.1047</u>	<u>24.75</u>	.8883	<u>.1320</u>
Lanczos	24.23	.8301	.1249	<u>21.24</u>	.7953	.1460	<u>24.04</u>	.8167	.1628	24.14	.8778	.1314	23.66	.8771	.1129	24.10	.8805	.1381
Bicubic	<u>24.13</u>	<u>.8275</u>	<u>.1263</u>	21.17	<u>.7954</u>	<u>.1453</u>	23.99	.8157	.1616	24.42	.8799	<u>.1293</u>	24.36	.8873	.1022	24.22	.8814	.1376
LiFT [25]	23.77	.8131	.1376	21.29	.7957	.1452	23.74	.8128	<u>.1619</u>	23.97	.8759	.1337	23.84	.8765	.1136	24.13	.8835	.1379
JAFAR [9]	23.79	.8163	.1362	20.03	.7681	.1713	24.01	<u>.8166</u>	.1624	24.32	.8803	.1313	23.95	.8810	.1090	24.26	.8823	.1377
AnyUp [29]	23.84	.8179	.1366	21.18	.7937	.1455	<u>24.04</u>	.8141	.1691	<u>24.44</u>	<u>.8806</u>	.1287	23.73	.8779	.1118	24.23	.8817	.1392

and NVS quality metrics (PSNR, SSIM, LPIPS), where positive values indicate that improved spectral behavior is associated with better reconstruction quality.

Across most interpolation and learned upsampling strategies, structural metrics (SSC and CSC) frequently exhibit positive correlations with reconstruction quality. In contrast, the high-frequency slope stability metric (HFSS) often shows negative correlations, indicating that stronger high-frequency spectral drift is associated with degraded reconstruction fidelity.

1.3 AG and AT Correlations

Additional geometry-only (AG) and texture-only (AT) correlation results are provided in Figs. 3, 5, 4, 6, and 7. These plots report Spearman correlations between spectral diagnostics and geometry-related ($-RPE_{mean}$) or texture-related ($-LPIPS$) reconstruction metrics across scenes. The results show consistent patterns with the main paper, the amplitude distribution metric ADC frequently

Table 2: Per-dataset NVS performance using MAST3R [20] with the DINO backbone. Results are reported on six multi-view datasets (LLFF, DL3DV, Casual, MipNeRF360, MVImgNet, and T&T) under three probing modes: Geometry-only, Texture-only, and All (geometry + texture). We evaluate PSNR (\uparrow), SSIM (\uparrow), and LPIPS (\downarrow). NSM denotes the no-upsampling baseline. Best results within each dataset and probing mode are highlighted in bold.

Upsamplers	LLFF									DL3DV								
	Geometry			Texture			All			Geometry			Texture			All		
	PSNR \uparrow	SSIM \uparrow	LPIPS \downarrow	PSNR \uparrow	SSIM \uparrow	LPIPS \downarrow	PSNR \uparrow	SSIM \uparrow	LPIPS \downarrow	PSNR \uparrow	SSIM \uparrow	LPIPS \downarrow	PSNR \uparrow	SSIM \uparrow	LPIPS \downarrow	PSNR \uparrow	SSIM \uparrow	LPIPS \downarrow
NSM	17.60	.8187	.1717	15.13	<u>.7452</u>	<u>.1924</u>	17.48	<u>.8140</u>	<u>.1707</u>	15.83	.7822	.2176	13.75	.6983	.2611	16.04	<u>.7866</u>	<u>.2243</u>
Bilinear	14.06	.7144	.2571	13.87	.7051	.2647	16.03	.7493	.2252	14.35	.7114	.2658	13.13	.6677	.2897	17.53	.7830	.2266
NN	16.85	.7931	.1808	15.12	.7463	.1902	17.31	.8060	.1802	16.19	.7817	.2213	13.67	.6961	.2633	15.81	.7755	.2259
Lanczos	15.17	.7256	.2290	15.19	.7250	.2523	<u>17.97</u>	.8126	.1723	15.87	.7641	.2317	13.70	.6976	.2620	15.44	.7838	.2251
Bicubic	15.21	.7397	.2091	14.74	.7228	.2251	15.60	.7492	.2036	15.77	.7587	.2323	14.96	.7321	.2470	16.06	.7689	.2319
LiFT [25]	15.55	.7431	.2201	14.33	.7115	.2479	16.12	.7586	.2272	15.97	.7413	.2293	13.74	.6984	.2702	16.63	.7903	.2307
JAFAR [9]	15.75	.7380	.2272	15.11	.7062	.2557	15.69	.7527	.1998	16.93	.7611	.2317	16.87	.7537	.2329	15.56	.7622	.2351
AnyUp [29]	13.58	.7004	.2585	15.27	.7264	.2507	18.22	.8227	.1701	14.68	.7220	.2564	13.73	.6980	.2614	16.13	.7800	.2295
Upsamplers	Casual									MipNeRF360								
	Geometry			Texture			All			Geometry			Texture			All		
	PSNR \uparrow	SSIM \uparrow	LPIPS \downarrow	PSNR \uparrow	SSIM \uparrow	LPIPS \downarrow	PSNR \uparrow	SSIM \uparrow	LPIPS \downarrow	PSNR \uparrow	SSIM \uparrow	LPIPS \downarrow	PSNR \uparrow	SSIM \uparrow	LPIPS \downarrow	PSNR \uparrow	SSIM \uparrow	LPIPS \downarrow
NSM	18.94	.7976	.2321	16.73	.7059	.2594	17.27	.7768	.2497	17.92	<u>.6721</u>	.3068	17.27	.6145	.2770	18.54	.6873	.2970
Bilinear	15.97	.7238	.2713	15.59	.6950	.2800	17.99	.7715	.2462	18.11	.6367	.2834	16.81	.5969	.2885	20.01	.6856	.2677
NN	16.70	.7546	.2594	16.70	.7041	.2604	17.62	.7802	.2428	19.71	.6842	.2779	17.24	.6138	.2771	16.92	.6314	.3524
Lanczos	19.14	.7796	.2262	17.39	<u>.7476</u>	<u>.2299</u>	17.18	.7599	.2615	18.48	.6497	.2634	18.09	.6215	<u>.2517</u>	18.54	.6836	.2986
Bicubic	19.52	.7851	.2218	18.29	.7448	.2358	18.94	.7869	.2370	18.08	.6318	.2794	17.15	.5998	.2780	18.27	.6490	.2962
LiFT [25]	18.77	.7803	.2219	15.47	.7017	.2667	16.75	.7597	.2544	18.06	.6395	.2736	17.76	.6097	.2653	19.41	.6823	.2866
JAFAR [9]	17.71	.7565	.2450	16.00	.7129	.2607	19.14	.7879	<u>.2402</u>	20.06	.6720	.2430	18.06	.6227	.2598	18.35	.6509	.2928
AnyUp [29]	18.74	.7849	.2199	17.41	.7496	.2293	16.68	.7548	.2649	19.91	.6609	<u>.2432</u>	18.16	<u>.6222</u>	.2500	18.49	.6809	.2923
Upsamplers	MVImgNet									T&T								
	Geometry			Texture			All			Geometry			Texture			All		
	PSNR \uparrow	SSIM \uparrow	LPIPS \downarrow	PSNR \uparrow	SSIM \uparrow	LPIPS \downarrow	PSNR \uparrow	SSIM \uparrow	LPIPS \downarrow	PSNR \uparrow	SSIM \uparrow	LPIPS \downarrow	PSNR \uparrow	SSIM \uparrow	LPIPS \downarrow	PSNR \uparrow	SSIM \uparrow	LPIPS \downarrow
NSM	18.50	.7717	.2196	17.26	.7089	<u>.2074</u>	18.24	.7693	.2130	18.43	.8086	.2056	17.38	.7993	.1920	19.99	.8570	.1727
Bilinear	18.60	.7442	.1933	16.93	.7048	.2137	19.32	.7623	.2013	19.00	<u>.8329</u>	.1807	17.00	.7873	.2061	18.71	.8253	.1969
NN	18.21	<u>.7605</u>	.2200	17.31	.7097	.2070	15.40	.7097	.2527	19.58	.8389	.1757	17.45	.7994	.1921	19.86	.8516	.1766
Lanczos	18.63	.7397	.1926	16.70	.7053	.2113	18.04	<u>.7672</u>	.2177	20.39	.8389	.1744	17.94	.7939	.1933	19.50	.8448	.1816
Bicubic	18.58	.7381	.1931	16.66	.7006	.2144	18.93	.7538	.2097	18.98	.8273	.1885	17.95	.7955	.1929	19.51	.8402	.1828
LiFT [25]	<u>19.02</u>	.7427	.1910	15.98	.6910	.2185	18.18	.7483	.2287	18.35	.8173	.1938	17.64	.7922	<u>.1916</u>	18.96	.8376	.1776
JAFAR [9]	18.96	.7440	.1881	16.61	.6938	.2140	<u>19.02</u>	.7550	<u>.2072</u>	18.44	.8136	.1963	17.32	.7816	.2096	18.88	.8350	.1866
AnyUp [29]	19.52	.7522	.1820	17.21	.7081	.2094	18.75	.7702	.2093	18.30	.8099	.2105	17.93	.7933	.1903	19.42	.8351	.1839

exhibits positive influence gaps across multiple interpolation and learned up-sampling methods, indicating stronger coupling with geometry-related reconstruction metrics. However, the magnitude of this effect varies depending on the backbone encoder and the 3D reconstructor. In contrast, the structural spectral consistency metrics (SSC and CSC) tend to influence texture fidelity slightly more than geometric accuracy but this trend can also be affected by the backbone encoder and the 3D reconstructor.

1.4 Geometry–Texture Gap

Additional geometry–texture influence gap results are provided in Figs. 8, 9, and 10. The gap plots illustrate whether a spectral diagnostic is more strongly associated with geometry- or texture-related reconstruction metrics across scenes. A positive Δ indicates stronger geometry coupling, whereas a negative value indicates stronger texture coupling.

Table 3: Per-dataset NVS performance using MAST3R [20] with the CLIP backbone. Results are reported on six multi-view datasets (LLFF, DL3DV, Casual, MipNeRF360, MVImgNet, and T&T) under three probing modes: Geometry-only, Texture-only, and All (geometry + texture). We evaluate PSNR (\uparrow), SSIM (\uparrow), and LPIPS (\downarrow). NSM denotes the no-upsampling baseline. Best results within each dataset and probing mode are highlighted in bold.

	LLFF									DL3DV								
	Geometry			Texture			All			Geometry			Texture			All		
Upsamplers	PSNR \uparrow	SSIM \uparrow	LPIPS \downarrow	PSNR \uparrow	SSIM \uparrow	LPIPS \downarrow	PSNR \uparrow	SSIM \uparrow	LPIPS \downarrow	PSNR \uparrow	SSIM \uparrow	LPIPS \downarrow	PSNR \uparrow	SSIM \uparrow	LPIPS \downarrow	PSNR \uparrow	SSIM \uparrow	LPIPS \downarrow
NSM	17.46	.8081	.1773	13.75	.7039	.2465	16.79	.7851	.1899	16.26	.7996	.2065	13.94	.7168	.2494	16.24	<u>.7976</u>	<u>.2136</u>
Bilinear	15.59	.7424	.2066	15.11	.7220	.2308	15.03	.7064	.2687	14.53	.7368	.2476	13.50	.6992	.2647	<u>16.50</u>	<u>.7489</u>	<u>.2376</u>
NN	<u>16.52</u>	<u>.7701</u>	<u>.2153</u>	<u>15.18</u>	<u>.7259</u>	<u>.2491</u>	<u>16.84</u>	<u>.7833</u>	<u>.1919</u>	16.82	.7947	.2127	13.88	.7146	.2523	16.17	.7987	.2115
Lanczos	14.19	.7220	.2489	14.38	.7190	.2206	16.19	.7781	.2049	15.36	.7411	.2489	14.06	.7157	.2538	17.04	.7968	.2181
Bicubic	14.71	.7246	.2354	14.36	.7111	.2467	16.19	.7567	.2300	14.39	.7139	.2592	13.37	.6793	.2740	14.50	<u>.7232</u>	<u>.2559</u>
LoftUp [15]	14.20	.7157	<u>.2359</u>	13.79	.7015	<u>.2550</u>	15.98	.7495	<u>.2078</u>	16.41	.7497	<u>.2383</u>	15.80	<u>.7348</u>	<u>.2390</u>	14.73	.7493	<u>.2422</u>
FeatUp [11]	16.19	.7602	<u>.1955</u>	17.26	.7514	.2154	18.30	<u>.7757</u>	<u>.1913</u>	14.84	.7072	.2706	15.16	.7431	.2330	15.95	<u>.7726</u>	<u>.2226</u>
JAFAR [9]	14.54	.6931	.2753	14.17	.6834	.2869	15.07	.7397	.2164	<u>16.50</u>	<u>.7423</u>	<u>.2374</u>	<u>15.40</u>	.7147	.2521	14.23	.7190	.2591
AnyUp [29]	14.82	.7344	.2021	14.31	.7182	<u>.2203</u>	16.48	.7817	.1977	15.12	.7468	<u>.2388</u>	14.13	.7172	<u>.2527</u>	16.27	.7859	<u>.2242</u>
	Casual									MipNeRF360								
Upsamplers	PSNR \uparrow	SSIM \uparrow	LPIPS \downarrow	PSNR \uparrow	SSIM \uparrow	LPIPS \downarrow	PSNR \uparrow	SSIM \uparrow	LPIPS \downarrow	PSNR \uparrow	SSIM \uparrow	LPIPS \downarrow	PSNR \uparrow	SSIM \uparrow	LPIPS \downarrow	PSNR \uparrow	SSIM \uparrow	LPIPS \downarrow
NSM	18.80	<u>.7906</u>	.2350	15.92	.6886	.2800	16.50	.7693	.2562	18.78	.6874	.2897	<u>18.02</u>	.6226	.2651	19.51	<u>.6919</u>	.2887
Bilinear	17.47	.7414	.2497	15.75	.6997	.2640	17.40	.7698	.2511	19.03	.6453	.2659	17.35	.6068	.2718	18.74	.6671	.2795
NN	17.81	.7609	.2507	16.04	.7006	.2685	17.58	.7821	<u>.2469</u>	19.77	<u>.6847</u>	.2810	18.42	<u>.6202</u>	.2565	18.80	.6909	.2931
Lanczos	<u>19.23</u>	<u>.7866</u>	<u>.2206</u>	<u>17.87</u>	<u>.7470</u>	.2352	17.62	.7638	.2526	18.69	.6515	.2663	17.05	.6021	.2792	19.14	.6873	.2845
Bicubic	16.37	.7303	.2677	15.58	.7022	.2747	17.81	<u>.7744</u>	.2457	<u>19.25</u>	.6615	.2471	17.61	.6192	<u>.2578</u>	19.67	.6788	.2851
LoftUp [15]	16.44	.7441	.2461	15.44	.7073	.2585	17.50	.7576	.2562	19.17	.6580	<u>.2531</u>	17.31	.6054	.2745	19.31	.6652	.2831
FeatUp [11]	19.68	.7939	.2080	16.40	.7045	.2574	17.31	.7556	.2585	18.68	.6445	.2644	17.51	.6061	.2691	18.90	.6538	<u>.2730</u>
JAFAR [9]	17.15	.7521	.2467	16.26	.7104	.2565	16.59	.7527	.2703	18.24	.6400	.2660	17.05	.6002	.2791	19.38	.6772	.2646
AnyUp [29]	18.91	.7777	<u>.2323</u>	17.91	.7471	<u>.2364</u>	<u>17.66</u>	.7652	.2504	18.76	.6476	.2620	17.03	.6018	.2797	20.13	.6932	.2814
	MVImgNet									T&T								
Upsamplers	PSNR \uparrow	SSIM \uparrow	LPIPS \downarrow	PSNR \uparrow	SSIM \uparrow	LPIPS \downarrow	PSNR \uparrow	SSIM \uparrow	LPIPS \downarrow	PSNR \uparrow	SSIM \uparrow	LPIPS \downarrow	PSNR \uparrow	SSIM \uparrow	LPIPS \downarrow	PSNR \uparrow	SSIM \uparrow	LPIPS \downarrow
NSM	18.12	.7663	.2133	15.81	.6773	.2280	18.35	.7593	.2156	20.08	.8544	.1671	18.44	.7997	.1844	20.71	.8614	.1665
Bilinear	18.94	.7471	.1893	16.81	.7025	.2103	20.59	.7754	.1894	18.70	.8155	.1948	17.62	.7830	.2161	19.14	.8315	.2005
NN	18.56	.7558	.2176	16.99	.6920	.2142	18.71	.7655	.2098	18.61	.8185	.2033	<u>17.74</u>	.7824	.2162	<u>20.46</u>	<u>.8572</u>	<u>.1705</u>
Lanczos	18.47	.7436	.1899	18.07	.7224	.1925	19.01	.7647	.2109	18.59	.8170	<u>.1837</u>	17.56	.7842	.2164	19.31	.8372	.1815
Bicubic	18.94	.7453	.1864	16.93	.7013	.2066	17.29	.7276	.2285	18.06	.8033	.2122	17.33	.7751	.2188	18.20	.8110	.2172
LoftUp [15]	18.97	.7471	.1854	16.81	.6999	.2088	<u>19.49</u>	.7659	.2020	18.24	.8052	.2068	17.11	.7760	.2143	18.62	.8239	.1991
FeatUp [11]	19.11	.7416	.1897	16.75	.7084	.2040	19.03	.7589	<u>.1985</u>	<u>19.28</u>	<u>.8246</u>	.1867	17.65	<u>.7875</u>	.2133	19.45	.8313	.1881
JAFAR [9]	20.25	.7579	.1708	17.93	.7118	.1963	19.25	.7591	.2006	19.19	.8234	.1963	17.47	.7868	<u>.2054</u>	18.22	.8149	.2133
AnyUp [29]	<u>20.22</u>	<u>.7643</u>	<u>.1747</u>	<u>18.04</u>	<u>.7223</u>	<u>.1932</u>	19.47	<u>.7700</u>	.2116	18.57	.8052	.2115	17.71	.7853	.2165	18.51	.8275	.1952

Across different upsampling strategies, the geometry–texture sensitivity varies considerably. Nevertheless, several consistent patterns can be observed.

First, the amplitude distribution metric ADC frequently exhibits positive gaps across multiple interpolation and learned upsampling methods, indicating stronger coupling with geometry-related reconstruction metrics. However, the magnitude of this effect varies depending on the backbone encoder and the 3D reconstructor.

Second, structural spectral consistency metrics (SSC and CSC) often show small or negative gaps, suggesting that structural spectral alignment tends to influence texture fidelity slightly more than geometric accuracy.

Finally, the influence gap can change substantially across different reconstructors. For example, the same spectral diagnostic may exhibit different magnitudes

or even sign changes when switching between DUST3R and MAST3R, suggesting that the relationship between spectral characteristics and reconstruction quality is strongly dependent on how the reconstructor utilizes feature representations.

References

1. Aydemir, G., Xie, W., Güney, F.: Can visual foundation models achieve long-term point tracking? arXiv preprint arXiv:2408.13575 (2024)
2. Bae, G., Davison, A.J.: Rethinking inductive biases for surface normal estimation. In: CVPR. pp. 9535–9545 (2024)
3. Barron, J.T., Mildenhall, B., Verbin, D., Srinivasan, P.P., Hedman, P.: Mip-nerf 360: Unbounded anti-aliased neural radiance fields. In: CVPR. pp. 5470–5479 (2022)
4. Bommasani, R.: On the opportunities and risks of foundation models. arXiv preprint arXiv:2108.07258 (2021)
5. Bonnen, T., Fu, S., Bai, Y., O’Connell, T., Friedman, Y., Kanwisher, N., Tenenbaum, J.B., Efros, A.A.: Evaluating multiview object consistency in humans and image models. In: NeurIPS. vol. 37, pp. 43533–43548 (2024)
6. Chen, B., Xu, Z., Kirmani, S., Ichter, B., Sadigh, D., Guibas, L., Xia, F.: SpatialVLM: Endowing vision-language models with spatial reasoning capabilities. In: CVPR. pp. 14455–14465 (2024)
7. Chen, H., Pei, Y., Zhao, H., Huang, Y.: Super-resolution guided knowledge distillation for low-resolution image classification. *Pattern Recognition Letters* **155**, 62–68 (2022)
8. Chen, Y., Chen, X., Chen, A., Pons-Moll, G., Xiu, Y.: Feat2gs: Probing visual foundation models with gaussian splatting. In: CVPR. pp. 6348–6361 (2025)
9. Couairon, P., Chambon, L., Serrano, L., Haugeard, J.E., Cord, M., Thome, N.: Jafar: Jack up any feature at any resolution. In: NeurIPS (2025)
10. El Banani, M., Raj, A., Maninis, K.K., Kar, A., Li, Y., Rubinstein, M., Sun, D., Guibas, L., Johnson, J., Jampani, V.: Probing the 3d awareness of visual foundation models. In: CVPR. pp. 21795–21806 (2024)
11. Fu, S., Hamilton, M., Brandt, L.E., Feldmann, A., Zhang, Z., Freeman, W.T.: Featup: A model-agnostic framework for features at any resolution. In: ICLR (2024)
12. Fu, X., Yin, W., Hu, M., Wang, K., Ma, Y., Tan, P., Shen, S., Lin, D., Long, X.: Geowizard: Unleashing the diffusion priors for 3d geometry estimation from a single image. In: ECCV. pp. 241–258 (2024)
13. Fu, X., Hu, Y., Li, B., Feng, Y., Wang, H., Lin, X., Roth, D., Smith, N.A., Ma, W.C., Krishna, R.: Blink: Multimodal large language models can see but not perceive. In: ECCV. pp. 148–166 (2024)
14. Hu, W., Gao, X., Li, X., Zhao, S., Cun, X., Zhang, Y., Quan, L., Shan, Y.: Depthcrafter: Generating consistent long depth sequences for open-world videos. In: CVPR. pp. 2005–2015 (2025)
15. Huang, H., Chen, A., Havrylov, V., Geiger, A., Zhang, D.: Loftup: Learning a coordinate-based feature upsampler for vision foundation models. In: ICCV. pp. 9913–9923 (2025)
16. Ke, B., Obukhov, A., Huang, S., Metzger, N., Daudt, R.C., Schindler, K.: Repurposing diffusion-based image generators for monocular depth estimation. In: CVPR. pp. 9492–9502 (2024)

17. Khirodkar, R., Bagautdinov, T., Martinez, J., Zhaoen, S., James, A., Selednik, P., Anderson, S., Saito, S.: Sapiens: Foundation for human vision models. In: ECCV. pp. 206–228 (2024)
18. Knapitsch, A., Park, J., Zhou, Q.Y., Koltun, V.: Tanks and temples: Benchmarking large-scale scene reconstruction. *ACM Transactions on Graphics (ToG)* **36**(4), 1–13 (2017)
19. Kopf, J., Cohen, M.F., Lischinski, D., Uyttendaele, M.: Joint bilateral upsampling. *ACM Transactions on Graphics (ToG)* **26**(3), 96–es (2007)
20. Leroy, V., Cabon, Y., Revaud, J.: Grounding image matching in 3d with mast3r. In: ECCV. pp. 71–91 (2024)
21. Ling, L., Sheng, Y., Tu, Z., Zhao, W., Xin, C., Wan, K., Yu, L., Guo, Q., Yu, Z., Lu, Y., et al.: D13dv-10k: A large-scale scene dataset for deep learning-based 3d vision. In: CVPR. pp. 22160–22169 (2024)
22. Linsley, D., Zhou, P., Ashok, A.K., Nagaraj, A., Gaonkar, G., Lewis, F.E., Pizlo, Z., Serre, T.: The 3d-pc: a benchmark for visual perspective taking in humans and machines. *arXiv preprint arXiv:2406.04138* (2024)
23. Mildenhall, B., Srinivasan, P.P., Ortiz-Cayon, R., Kalantari, N.K., Ramamoorthi, R., Ng, R., Kar, A.: Local light field fusion: Practical view synthesis with prescriptive sampling guidelines. *ACM Transactions on Graphics (ToG)* **38**(4), 1–14 (2019)
24. Örnek, E.P., Labbé, Y., Tekin, B., Ma, L., Keskin, C., Forster, C., Hodan, T.: Foundpose: Unseen object pose estimation with foundation features. In: ECCV. pp. 163–182 (2024)
25. Suri, S., Walmer, M., Gupta, K., Shrivastava, A.: Lift: A surprisingly simple lightweight feature transform for dense vit descriptors. In: ECCV. pp. 110–128 (2024)
26. Tan, W., Yan, B., Bare, B.: Feature super-resolution: Make machine see more clearly. In: CVPR. pp. 3994–4002 (2018)
27. Tumanyan, N., Singer, A., Bagon, S., Dekel, T.: Dino-tracker: Taming dino for self-supervised point tracking in a single video. In: ECCV. pp. 367–385 (2024)
28. Wang, S., Leroy, V., Cabon, Y., Chidlovskii, B., Revaud, J.: Dust3r: Geometric 3d vision made easy. In: CVPR. pp. 20697–20709 (2024)
29. Wimmer, T., Truong, P., Rakotosaona, M.J., Oechsle, M., Tombari, F., Schiele, B., Lenssen, J.E.: Anyup: Universal feature upsampling. *arXiv preprint arXiv:2510.12764* (2025)
30. Ye, C., Qiu, L., Gu, X., Zuo, Q., Wu, Y., Dong, Z., Bo, L., Xiu, Y., Han, X.: Stablenormal: Reducing diffusion variance for stable and sharp normal. *ACM Transactions on Graphics (TOG)* **43**(6), 1–18 (2024)
31. Yu, X., Xu, M., Zhang, Y., Liu, H., Ye, C., Wu, Y., Yan, Z., Zhu, C., Xiong, Z., Liang, T., et al.: Mvimnet: A large-scale dataset of multi-view images. In: CVPR. pp. 9150–9161 (2023)
32. Zuo, Y., Kayan, K., Wang, M., Jeon, K., Deng, J., Griffiths, T.L.: Towards foundation models for 3d vision: How close are we? In: 3DV. pp. 1285–1296 (2025)

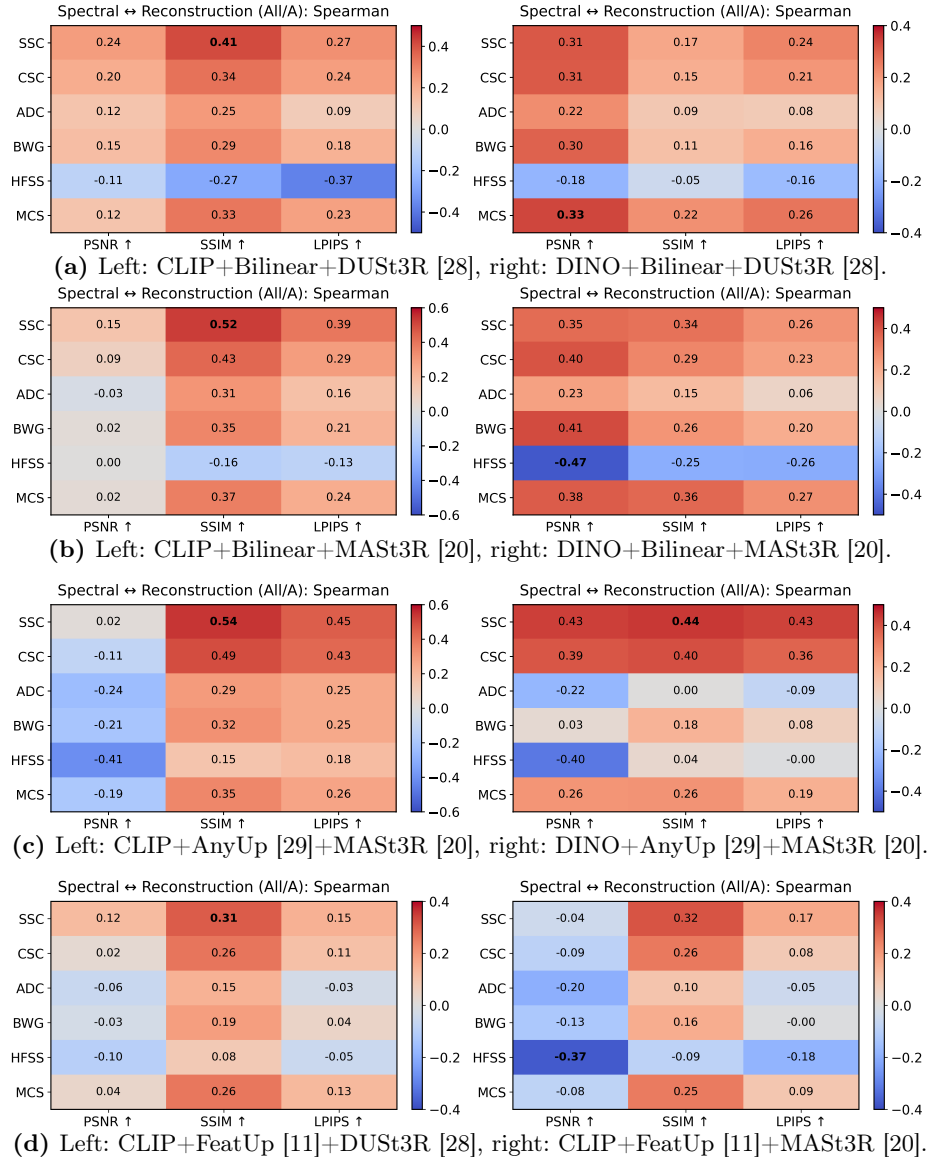


Fig. 1: Spectral-reconstruction correlations. Each row shows the Spearman correlation heatmap.

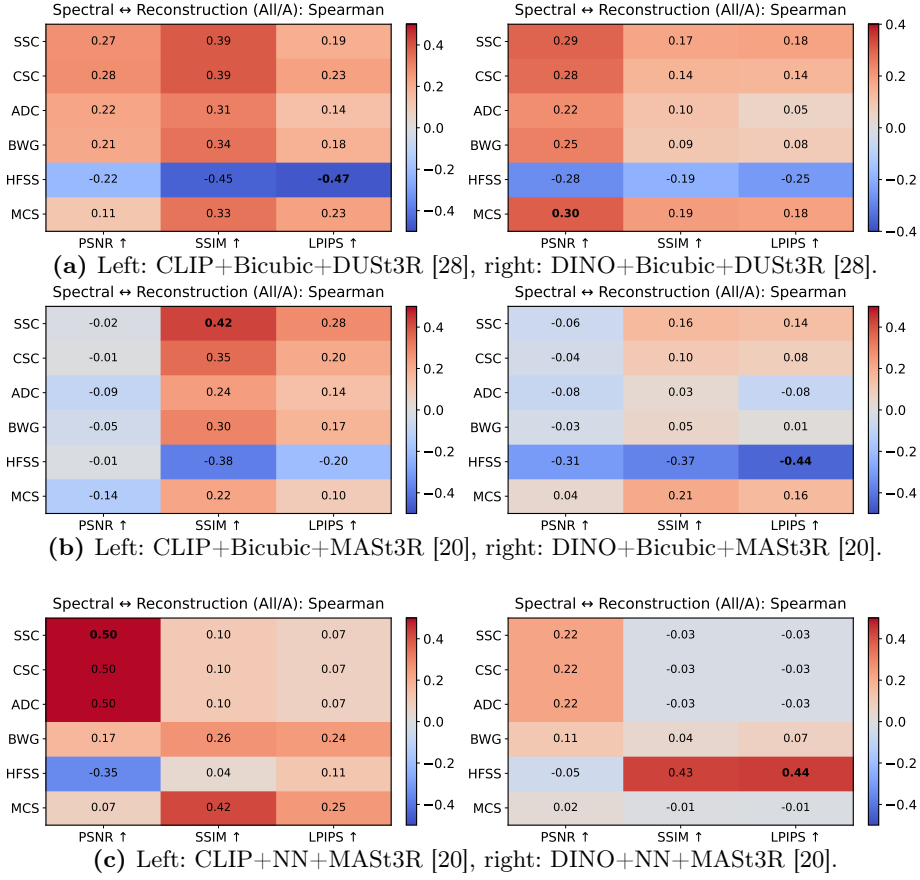


Fig. 2: Spectral–reconstruction correlations. Each row shows the Spearman correlation heatmap.

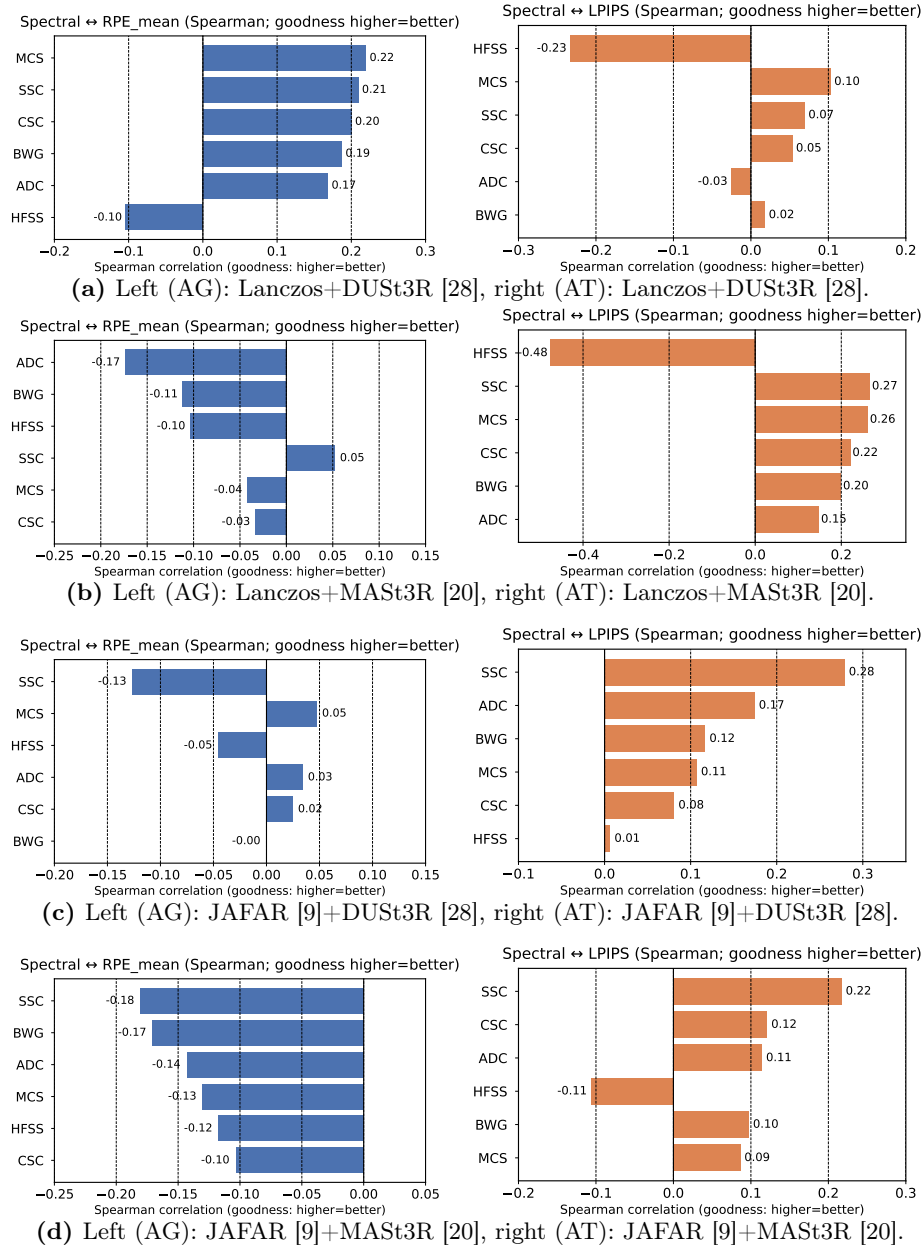


Fig. 3: Spearman correlations between spectral diagnostics and reconstruction quality under geometry-only (AG) and texture-only (AT) probing settings (DINO). Left panels show correlations with $-RPE_{mean}$ (geometry quality), and right panels show correlations with $-LPIPS$ (texture quality).

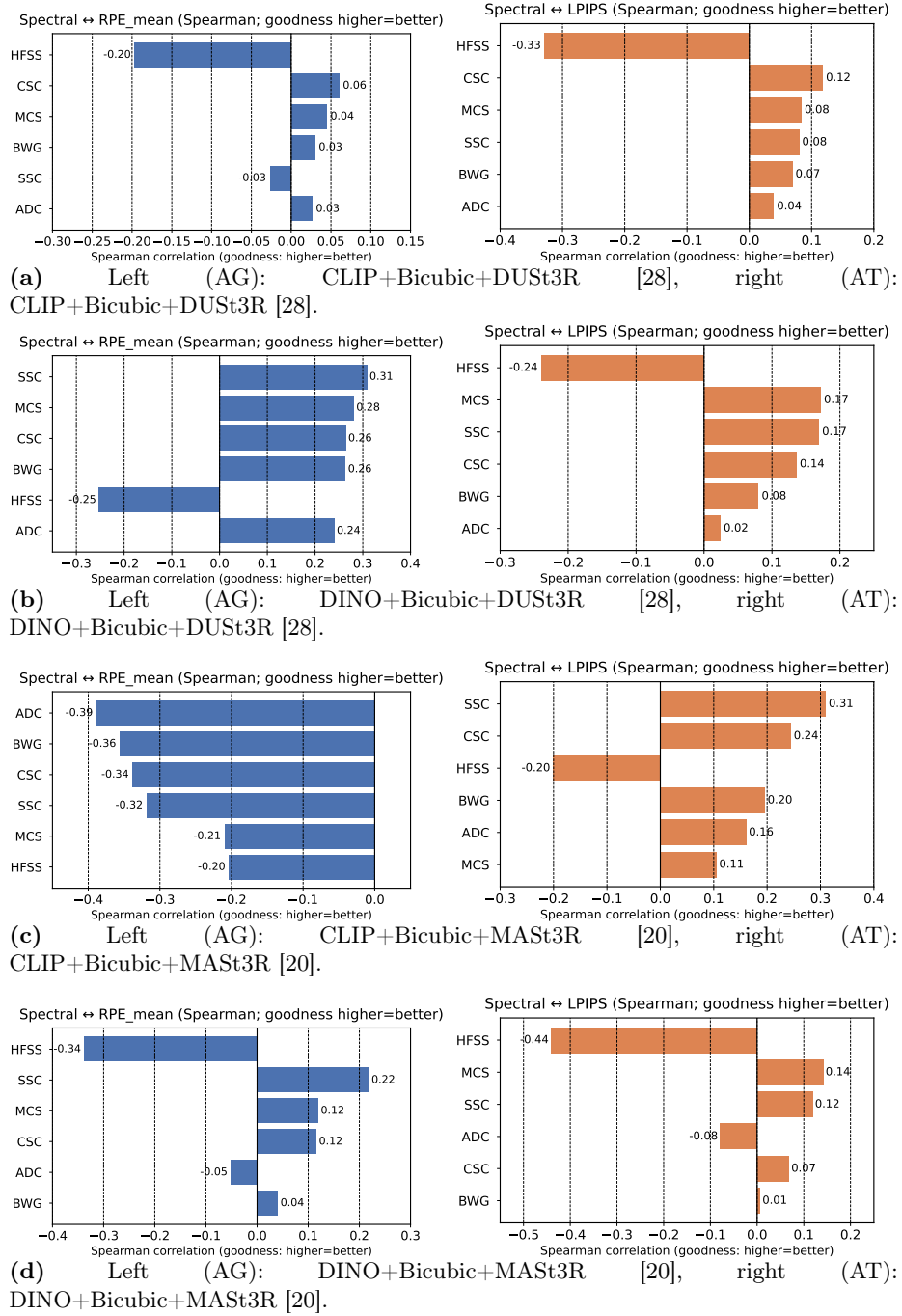


Fig. 4: Spearman correlations between spectral diagnostics and reconstruction quality under geometry-only (AG) and texture-only (AT) probing settings. Left panels show correlations with $-RPE_{mean}$ (geometry quality), and right panels show correlations with $-LPIPS$ (texture quality).

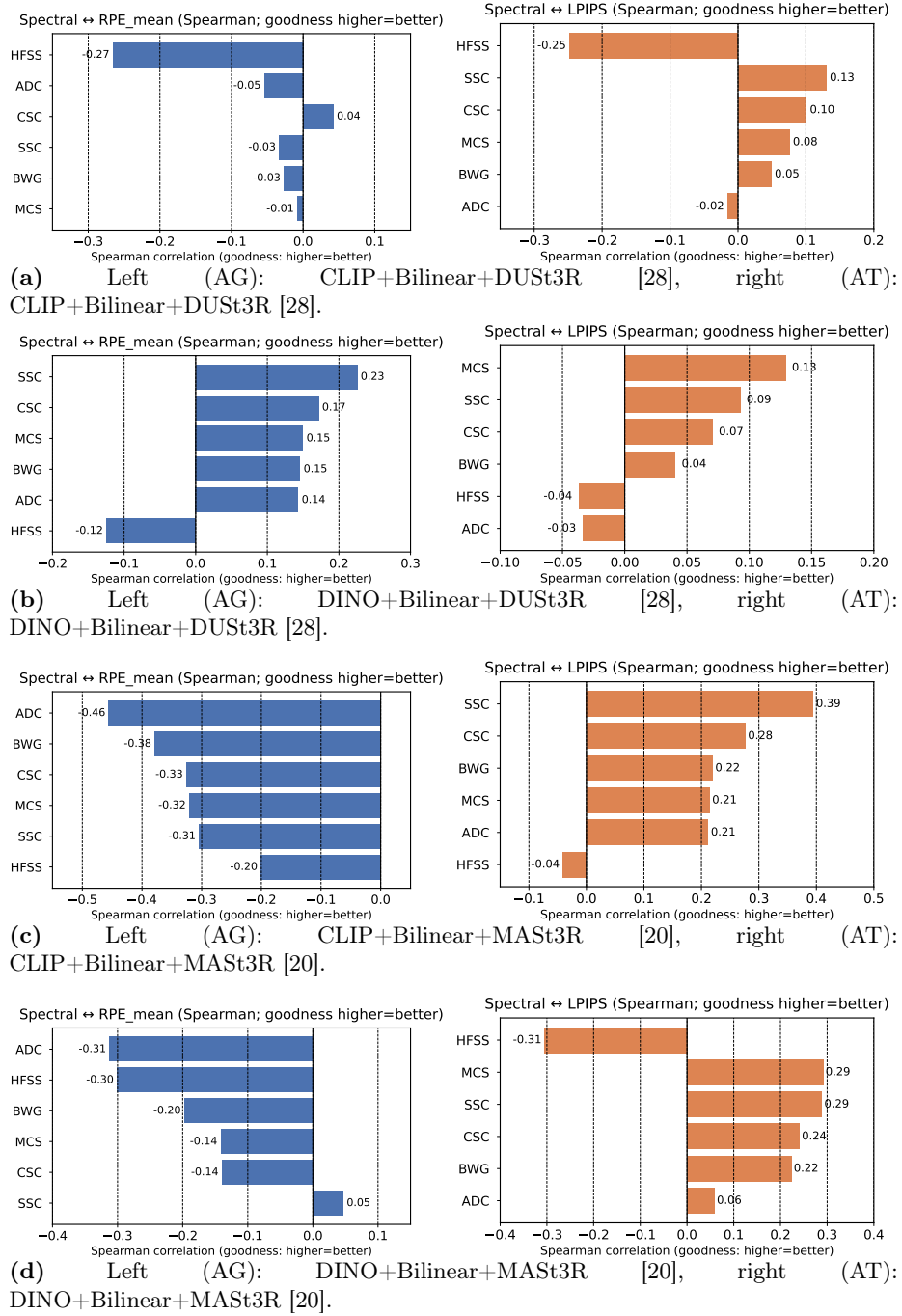


Fig. 5: Spearman correlations between spectral diagnostics and reconstruction quality under geometry-only (AG) and texture-only (AT) probing settings. Left panels show correlations with $-RPE_{mean}$ (geometry quality), and right panels show correlations with $-LPIPS$ (texture quality).

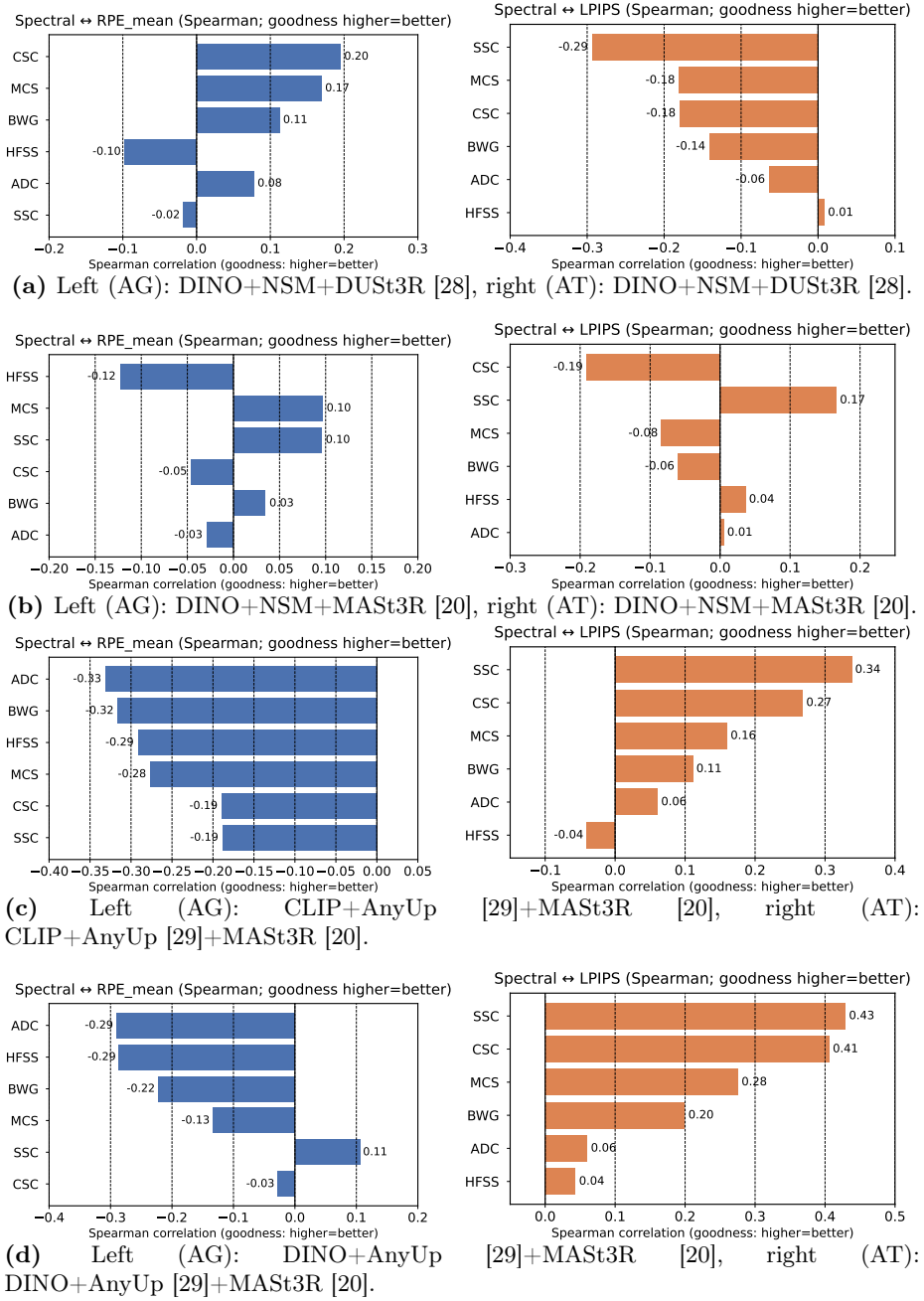


Fig. 6: Spearman correlations between spectral diagnostics and reconstruction quality under geometry-only (AG) and texture-only (AT) probing settings. Left panels show correlations with $-RPE_{mean}$ (geometry quality), and right panels show correlations with $-LPIPS$ (texture quality).

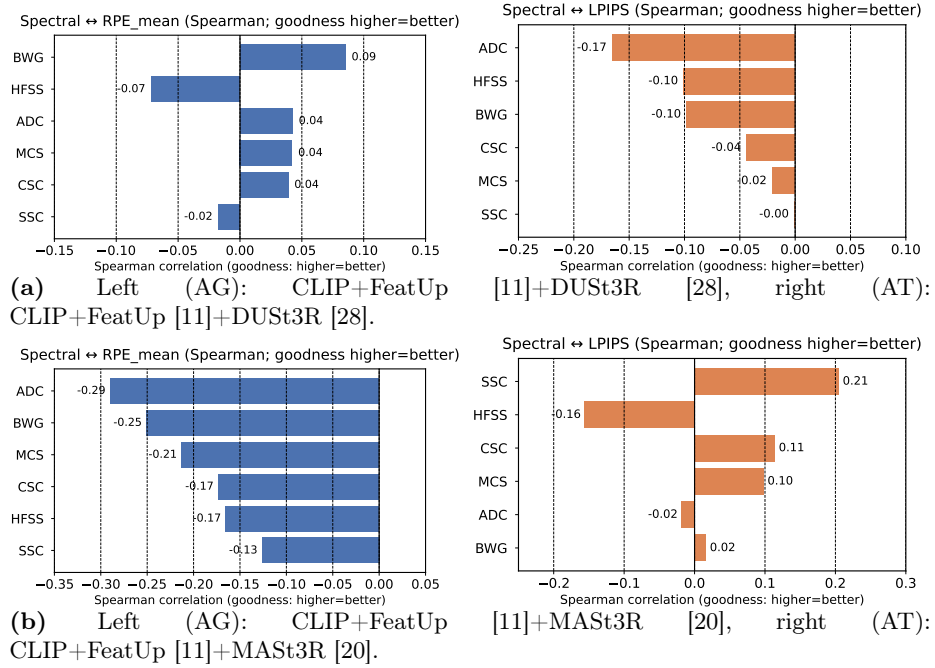


Fig. 7: Spearman correlations between spectral diagnostics and reconstruction quality under geometry-only (AG) and texture-only (AT) probing settings. Left panels show correlations with $-RPE_{mean}$ (geometry quality), and right panels show correlations with $-LPIPS$ (texture quality).

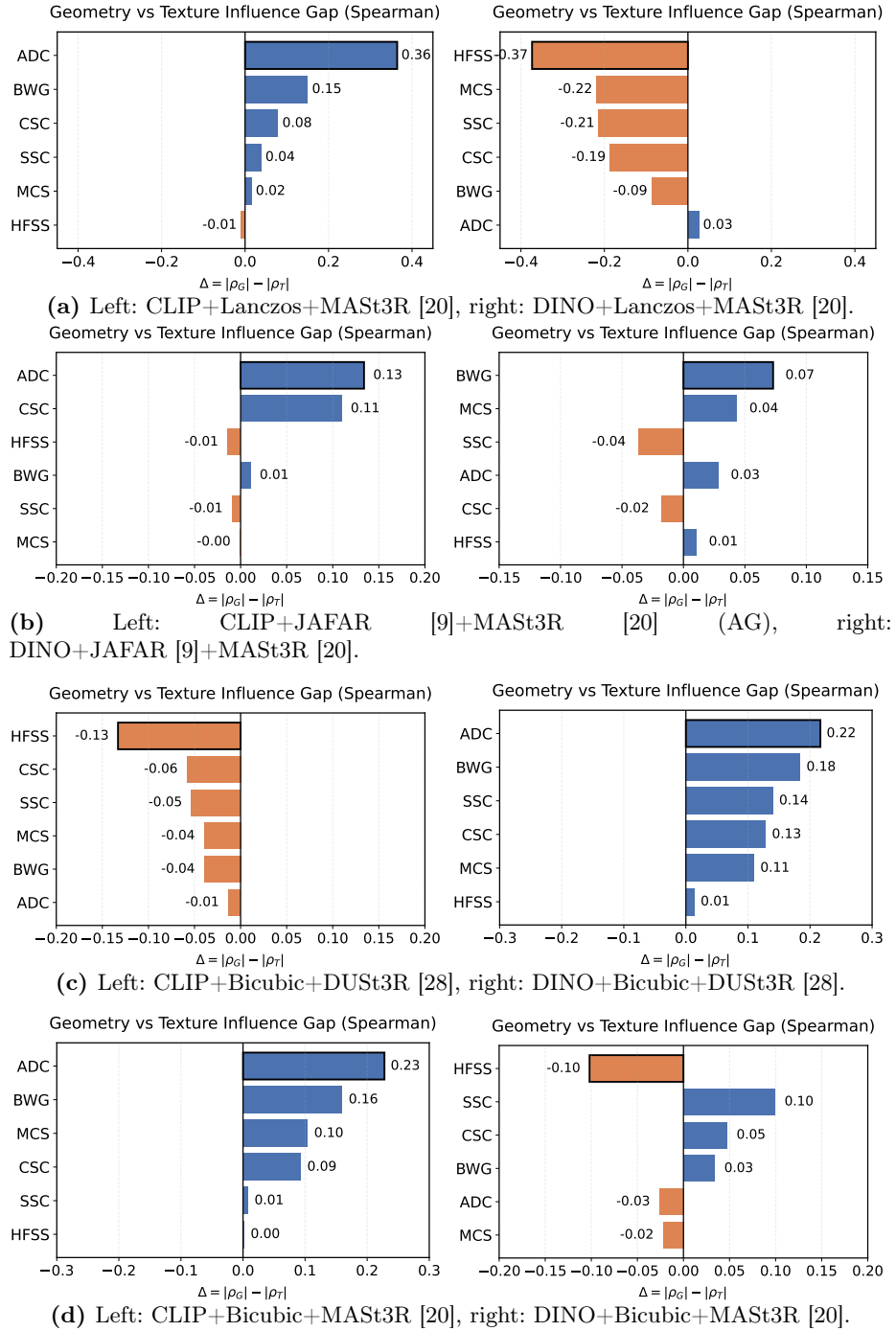


Fig. 8: Geometry-texture influence gap.

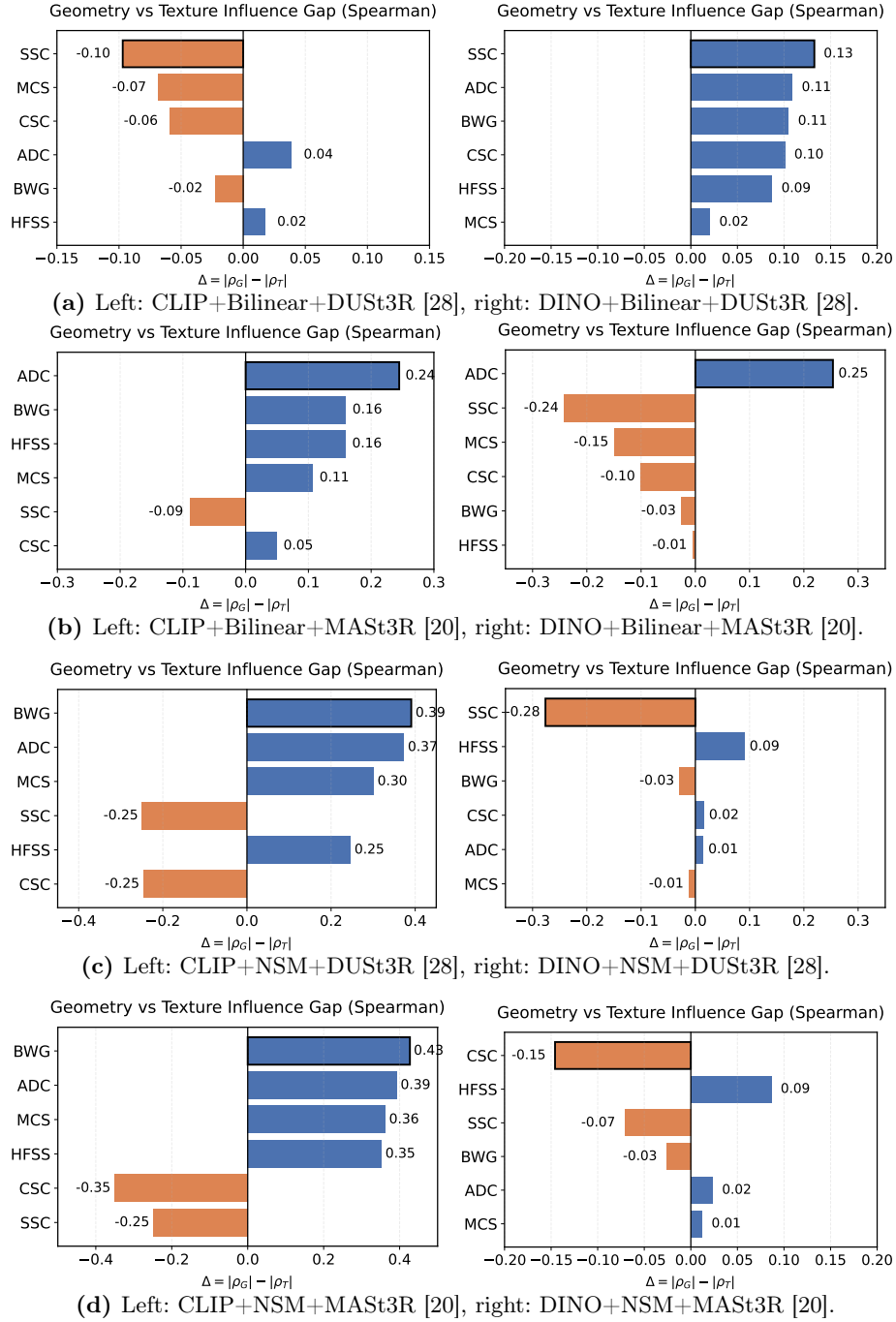


Fig. 9: Geometry–texture influence gap.

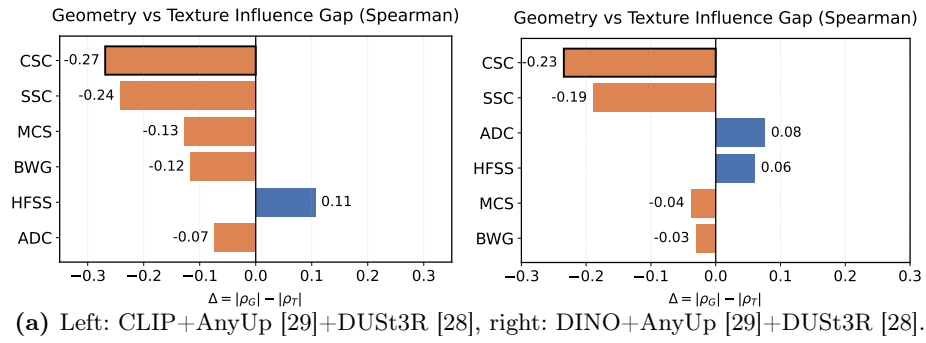


Fig. 10: Geometry–texture influence gap.